MATERIALS SCIENCE

An antiswelling biodegradable hydrogel reshapes electro-microenvironment to drive endogenous neuroregeneration after brain defect

Zhen Luo[1,2]†, Meng Xiao[3,4]†, Jing Huang[4]†, Rong Yang[1,2], Xinrui Zhao[1,2], Jiaxing Shao[1,2], Jian Cheng[4], Chunyan Cui[1,2]*, Zhou Li[3,5]*, Wenguang Liu[1,2]*

Bioactive matrix filling is a promising strategy for treating acute traumatic brain injury (TBI)–related substantial brain defects, requiring a dual-functional matrix that resists swelling and remodels microenvironments for endogenous regeneration. Herein, we design an antiswelling, biodegradable adhesive hydrogel through supramolecular self-assembly of two Food and Drug Administration–approved drugs (lipoic acid and metformin) via multi-hydrogen bonding with precise regulation of solution pH. This hydrogel matrix recapitulates critical native brain tissue characteristics, including mechanical and electrical compatibility. During degradation, released lipoic acid remodels the injury site into a proregenerative niche, while metformin promotes spontaneous recruitment of endogenous neural stem cells (NSCs) to defect area. Integrated with a flexible cortical electrode and exogenous electrical stimulation, this system further directs NSC differentiation into functional neurons. In a substantial brain defect rat model, this strategy achieves a 14.8-fold increase in NSC recruitment and an 11.3-fold enhancement in neuronal differentiation, leading to a 78% reduction in tissue defect volume and notable functional recovery. This work establishes a therapeutic paradigm for endogenous repair after TBI.

INTRODUCTION

Acute traumatic brain injury (TBI) arises from violent external mechanical impacts to the head, which directly disrupts brain tissue and impairs neurological function, frequently resulting in focal tissue loss and necrotic cavity formation (*1*). Promoting brain tissue regeneration and activating neural network reconstruction and synaptic renewal within these cavities are critical for treating post-TBI substantial brain defects (*2*). However, this is severely limited by the adult brain's poor regenerative capacity and inadequate endogenous repair mechanisms. A central challenge lies in the hostile injury microenvironment at the TBI site, which results in insufficient recruitment of endogenous neural stem cells (NSCs) and aberrant activation of glial cells (*3*). The transplantation of exogenous NSCs is considered a promising yet challenging strategy for TBI repair (*4*–*7*); However, its clinical translation is plagued by several issues: limited cell sources, low viability, suboptimal neuronal differentiation, and immune rejection (*8*–*10*). Crucially, it also fails to address the cavity itself, providing no structural support or scaffold to guide functional neural circuit reconstruction. Active biomaterials, with their advanced capabilities in microenvironment regulation, represent a rapidly evolving frontier. Their local implantation offers a compelling alternative to remodel the neural niche, enabling the in situ recruitment of autologous NSCs and their subsequent differentiation into neurons for repairing substantial post-TBI brain defects.

However, two major obstacles hinder the application of brain-implantable materials: uncontrolled swelling in the hydrophilic cerebral environment and a degradation rate that fails to match the pace of neural regeneration (*11*, *12*). Excessive swelling can cause tissue compression and cerebral edema (*13*, *14*). In contrast, overly rapid degradation fails to provide long-term mechanical support, and excessively slow degradation impedes brain tissue regeneration and neural circuit reconstruction. Here, we aim to design and develop an active, instructive biomaterial matrix that can fill the defect and guide endogenous neural regeneration, addressing the critical challenges in treating substantial brain defects. The design of such a material should meet several key criteria: First, it must achieve a critical balance between structural stability and controlled degradation. This balance is essential to both maintain mechanical support for the defect cavity and to progressively create a permissive environment for regenerative tissue and neural circuits. Second, the material's mechanical properties must closely match those of native brain tissue to avoid mismatch-induced secondary injury (*15*, *16*). Third, the material must exhibit conductivity comparable to native brain tissue to facilitate electrophysiological signal transmission and neural activity (*17*). This feature would not only provide electrical cues to guide neuronal growth and synaptic formation but also enable the integration of exogenous electrical stimulation (ES) to enhance the directed differentiation of NSCs toward neuronal lineages (*18*–*21*). Fourth, it must leverage its inherent microenvironment-modulating capability and ensure high biocompatibility to support feasible clinical translation.

In accordance with these criteria, we engineered the α-lipoic acid (LA) and metformin (Met) self-assembled (LMSA) hydrogel matrix: an injectable, antiswelling, biodegradable, and bioactive supramolecular adhesive designed to serve as an instructive regenerative matrix for treating substantial brain defects following acute TBI (Fig. 1). This design enables a paradigm shift from conventional passive, static scaffolds to a smart, active therapeutic system capable of adaptive, stimulus-responsive therapeutic action. In contrast to conventional strategies that typically rely on drug encapsulation within preformed hydrogels, synthetic cross-linkers, or the incorporation of conductive fibers/inorganic additives to impart electrical functionality, the LMSA

[1]School of Materials Science and Engineering, Tianjin University, Tianjin 300350, China. [2]Tianjin Key Laboratory of Composite and Functional Materials, Tianjin University, Tianjin 300350, China. [3]Vita Tech Innovation Center, Tsinghua Changgung Hospital, School of Clinical Medicine, Tsinghua University, Beijing, 100084, China. [4]Beijing Institute of Nanoenergy and Nanosystems, Chinese Academy of Sciences, Beijing 101400, China. [5]School of Biomedical Engineering, Tsinghua University, Beijing 100084, China. *Corresponding author. Email: cycui@tju.edu.cn (C.C.); li_zhou@tsinghua.edu.cn (Z.L.); wgliu@tju.edu.cn (W.L.)
†These authors contributed equally to this work.

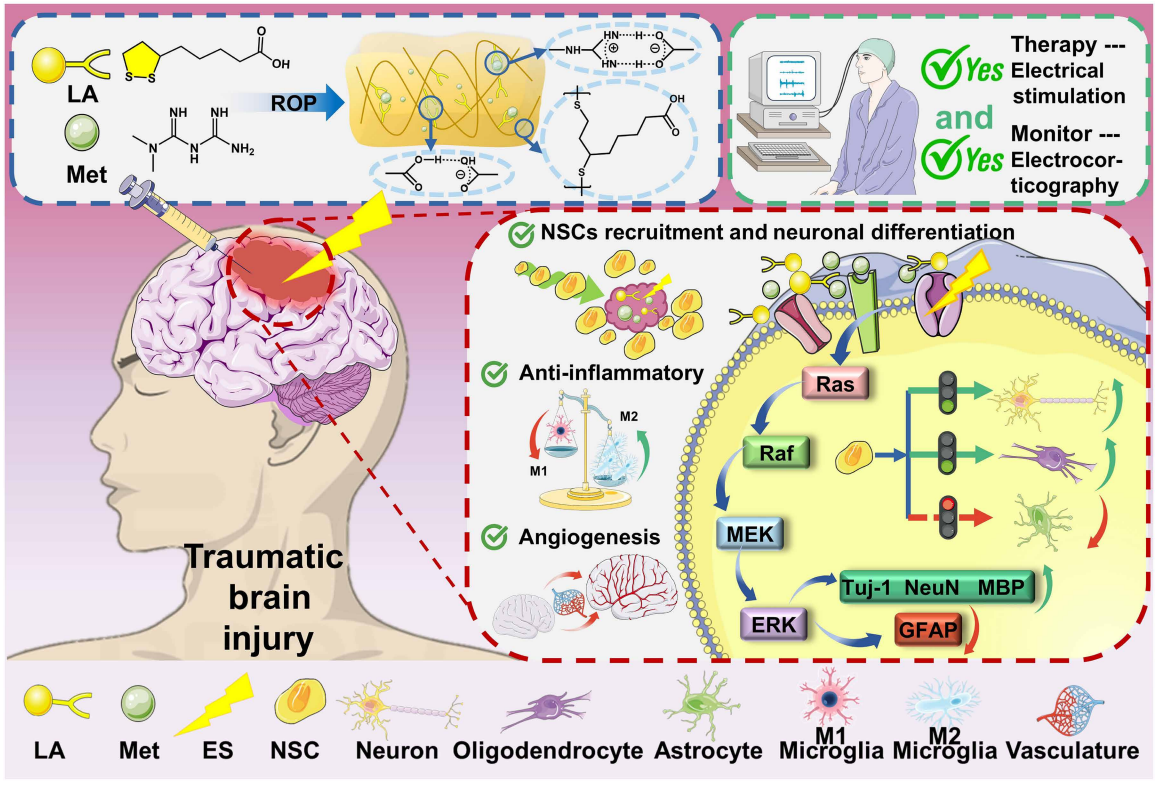

Fig. 1. Design and implementation of the LMSA hydrogel combined with an ES strategy. Schematic illustration of the construction of the LMSA hydrogel and its integration with ECoG electrodes for ES and signal monitoring after TBI. The system synergistically recruits and induces endogenous NSCs toward neuronal differentiation, while suppressing neuroinflammation and promoting vascularization, thereby enabling multifunctional brain repair. Created in BioRender. luo, Z. (2026) https://BioRender.com/1zpqkhj.

hydrogel designed herein is fabricated exclusively from two Food and Drug Administration–approved pharmaceutical agents through dynamic, multi-hydrogen bond–mediated supramolecular self-assembly. This constitutes a conceptually distinct and fundamentally previously unidentified paradigm in supramolecular biomaterial engineering, in which the therapeutic drugs themselves act simultaneously as structural building blocks, dynamic cross-linkers, bioactive agents, and intrinsic conductivity components without relying on exogenous molecules. The inherent alkalinity of Met partially deprotonated LA, enhancing its aqueous solubility and triggering spontaneous ring-opening polymerization of concentrated LA to form PolyLA. The hydrophobic PolyLA backbone provided structural stability and swelling resistance in physiological environments, while its disulfide–cross-linked network allowed for controlled degradation by endogenous reducing agents. Moreover, by tuning the LA-to-Met ratio, the matrix could be tailored to match the mechanical properties of native brain tissue. In addition, the protons generated from deprotonation served as effective charge carriers, endowing the material with brain tissue–level conductivity. Integrated with a flexible electrocorticography (ECoG) electrode, LMSA synergized with ES to treat substantial brain defects induced by acute TBI. The injectable LMSA adhesive seamlessly filled irregular defect cavities and securely anchored the flexible electrode. Sustained local release of LA effectively remodeled the pathological microenvironment, reshaping a proregenerative niche. In contrast, Met release recruited autologous NSCs in situ via activation of the AMPK signaling pathway and up-regulation of brain-derived neurotrophic factor expression (*22*–*24*); this process, aided by ES, further promoted the directed differentiation of these NSCs into neurons. In NSC culture, the hydrogel combined with ES significantly increased the efficiency of NSC differentiation into neurons from 45 to 80%. A rat model of substantial traumatic brain defect was established by inducing a severe head impact, and the hydrogel matrix integrated with a flexible electrode was implanted to fill the defect area. When combined with exogenous ES, this treatment notably accelerated brain tissue regeneration, resulting in notable improvements across histological, behavioral, and electrophysiological measures. Moreover, beyond enabling a "recruitment-differentiation" cascade, this electrically stimulated active regenerative matrix establishes an integrated platform for TBI treatment and neurological recovery monitoring—a transformative strategy for personalized neural repair that bridges materials science and clinical neurology.

RESULTS

Preparation and characterization of LMSA hydrogels

The inherent hydrophobicity of LA restricts its solubility in water, whereas the intrinsic alkalinity of Met notably enhances it by deprotonating LA. We observed that the degree of deprotonation of LA by Met substantially influences the state of the resulting product. As shown in the phase diagram (Fig. 2, A and B), increasing the Met content drives the system to undergo sequential transitions into precipitation, hydrogel, and homogeneous aqueous solution. Therefore, we first used the Henderson-Hasselbalch equation to calculate the extent of deprotonation of the carboxyl groups in LA at different

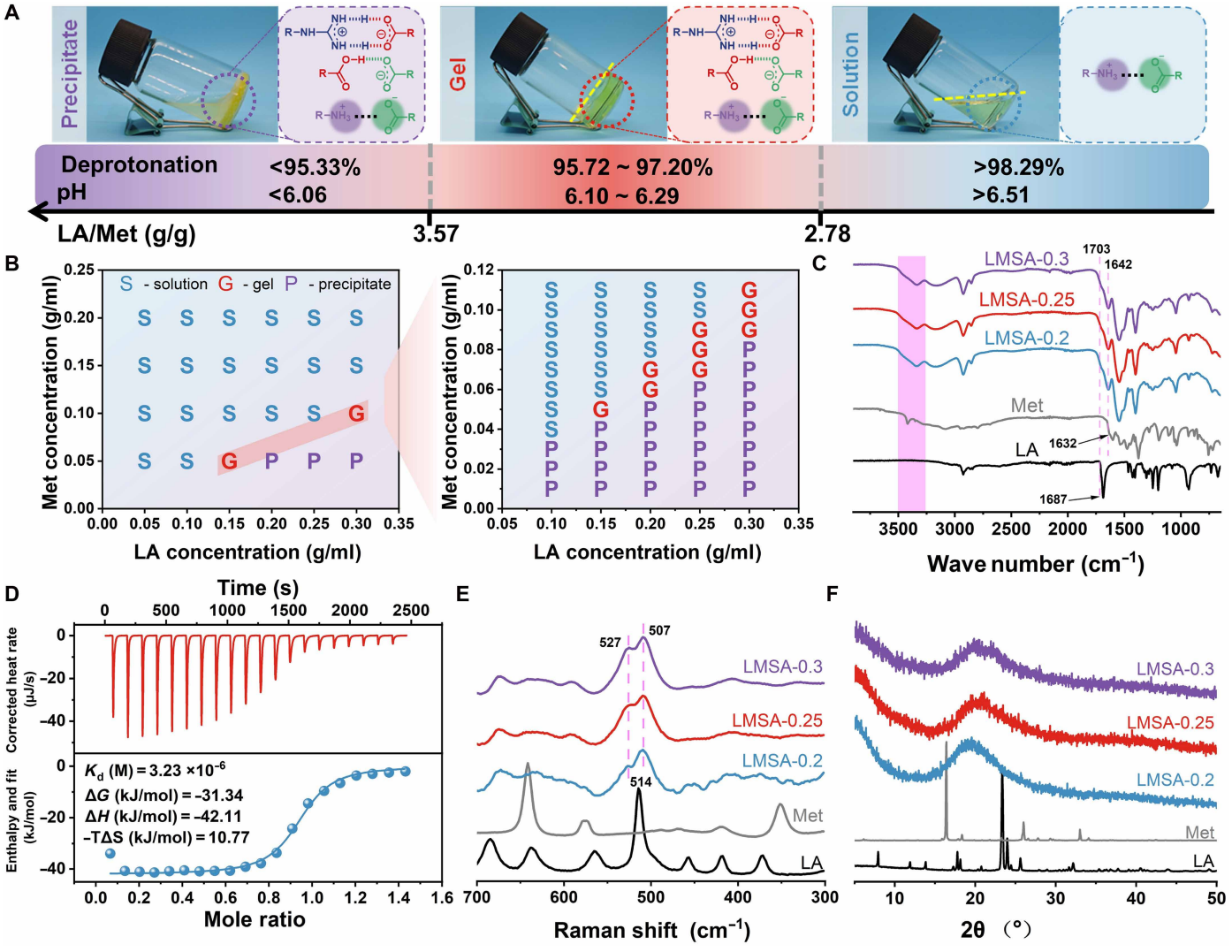

Fig. 2. Characterization of LMSA hydrogels. (**A**) Digital photos showing the gelation ability of LA and Met aqueous solutions with different compositions. (**B**) Phase diagram of different concentrations of LA and Met. (**C**) FTIR spectra of the LA, Met, and LMSA hydrogels with different compositions. (**D**) ITC raw data fitted curves and thermodynamic parameters of LA titrated with Met. (**E**) Raman spectra of the LA, Met, and LMSA hydrogels with different compositions. (**F**) XRD patterns of the LA, Met, and LMSA hydrogels with different compositions.

compositions by measuring their pH values. As presented in fig. S1, a hydrogel forms only when the deprotonation degree of LA is precisely controlled between 95.72 and 97.2% (corresponding to an LA-to-Met mass ratio ranging from 3.6:1 to 2.8:1, a molar ratio from 2.2:1 to 1.7:1, and a mixture pH of 6.10 to 6.29). In this state, LA is fully solubilized via ion-pair formation between deprotonated LA anions and protonated Met cations. Driven by the high-concentration aggregation–induced ring-opening polymerization of LA, along with ionic hydrogen bonds (carboxyl/carboxylate), salt-bridge hydrogen bonds (carboxyl/guanidyl), and electrostatic interactions, the system then spontaneously self-assembles into a hydrogel. In contrast, at a lower degree of deprotonation, insoluble LA persists as a precipitate even in the presence of these interactions. When the Met content is higher, near-complete deprotonation achieves full solubilization of LA but raises the pH, which disrupts hydrogen bonding and thereby inhibits self-assembly. Subsequently, we fixed the mass ratio of Met to LA at 3:1 for hydrogel fabrication and examined the effect of varying the total solid content on the hydrogel properties. The resulting hydrogels were designated as LMSA-x, where x represents the solid content of LA in the system. Detailed hydrogel preparation procedures are provided in the Supplementary Materials (fig. S2). Fourier transform infrared spectroscopy (FTIR) showed that in the LMSA hydrogel (Fig. 2C), the carboxyl C=O peak of LA shifts from 1687 to 1703 cm^{-1}, the C=N absorption peak of Met shifts from 1632 to 1642 cm^{-1}, and the N–H stretching vibration peak becomes notably broader. These spectral changes further confirm the formation of strong ionic hydrogen bonds (between carboxylate groups of deprotonated LA and carboxyl groups of LA) and salt-bridge hydrogen bonds (between carboxyl groups of LA and guanidinium groups of Met) in the hydrogel (*25*–*27*).

To further elucidate the molecular interactions between LA and Met in the homogeneous hydrogel phase, we conducted thermodynamic analysis using isothermal titration calorimetry (ITC). The titration of LA with Met yielded a downward, exothermic curve

(Fig. 2D), indicative of a spontaneous process characterized by a favorable enthalpy change ($\Delta H < 0$) and an overall negative free energy change ($\Delta G < 0$). The notably larger value of $|\Delta H|$ compared to $|T\Delta S|$, coupled with a positive $-T\Delta S$ value, suggests that the enthalpic contribution overcomes the entropic contribution (*28*, *29*). This confirms that the interaction between LA and Met is primarily enthalpy driven, consistent with a binding mechanism facilitated by specific hydrogen bonding. The intermolecular affinity was further characterized by the dissociation constant (K_d). The measured K_d of 3.23×10^{-6} M signifies strong (micromolar) binding (*30*), unequivocally confirming that the association is a specific chemical event driven by spontaneous hydrogen bonding, rather than a result of physical blending (*31*). The characteristic Raman peak of the disulfide bond at 514 cm^{-1} in the LA monomer splits into two peaks at 507 and 527 cm^{-1} in the LMSA hydrogels, indicating that the disulfide five-membered ring in LA monomers undergoes ring-opening polymerization within the hydrogel system (Fig. 2E) (*32*). X-ray diffraction (XRD) patterns revealed that, in contrast to the sharp crystalline peaks of pure LA and Met, the LMSA hydrogel exhibited a broad amorphous pattern. This observation further confirms the occurrence of ring-opening polymerization of LA (Fig. 2F) (*33*). It also indicates that the introduction of Met stabilizes the resulting PolyLA network.

Mechanical and adhesive properties of LMSA hydrogels

Given the prerequisite for mechanical strength matching that of brain tissue in repair materials, we characterized the LMSA hydrogel using rheological tests. The time sweep results confirmed a robust gel state, with the storage modulus (G′) persistently surpassing the loss modulus (G″) (Fig. 3A). The observed increase in both moduli with elevated solid content directly points to an augmented cross-linking density within the hydrogel network. Angular frequency sweep tests revealed that at 100 rad/s—a frequency close to the body's intrinsic rhythm—the storage modulus of the LMSA hydrogel falls within the range of natural brain tissue (0.2 to 3.1 kPa) (Fig. 3B) (*34*). A tissue-matching modulus is critical in vivo as it minimizes mechanical damage to the surrounding environment. Moreover, previous studies have demonstrated that softer materials (0.1 to 1 kPa) preferentially promote neuronal differentiation, while stiffer materials (7.0 to 10 kPa) tend to promote glial cell differentiation (*35*). Therefore, this suitable modulus positions the LMSA hydrogel as a promising neural scaffold for TBI repair. Moreover, the viscosity of LMSA hydrogel decreases with increasing shear rate (Fig. 3C), demonstrating typical shear-thinning behavior, which allows it to be easily extruded through a syringe and patterned into intricate shapes (fig. S3). This injectability behavior is attributed to the abundance of dynamic hydrogen bonds and reversible disulfide cross-links within the hydrogel network, and it is crucial for localized delivery and the effective filling of the brain injury site.

Given the complex pathological microenvironment after TBI and the presence of cerebrospinal fluid perfusing the site of substantial brain tissue defects, it is crucial for the hydrogel implanted into the brain defect to maintain its structural integrity and resist swelling, thereby providing effective physical filling and support while avoiding collapse and tissue compression. To simulate the environment of a brain defect, we immersed LMSA in artificial cerebrospinal fluid (ACSF). In the initial stage of immersion, LMSA exhibited negligible swelling (the maximum swelling volume is 30% greater than the initial volume) due to the infiltration of water molecules from the ACSF into the hydrogel network (fig. S4). As immersion time increased, the volume of LMSA ultimately returned to its initial state, which may be attributed to further hydrophobic aggregation of PolyLA induced by water molecules in the ACSF. To further assess the in vivo safety of the LMSA hydrogel, we created a cylindrical defect (8-mm diameter and 6-mm depth) in ex vivo pig and goat brains, followed by hydrogel injection into the defects. The samples were fully immersed in ACSF for 7 days, and defect diameters were measured at various time points (figs. S5 and S6). Results showed that hydrogel injection into the defects did not induce significant changes in defect diameter compared to controls, indicating that LMSA effectively resists swelling, maintains long-term structural stability, and avoids local compression of injured brain tissue.

The balance between early-stage mechanical support and mid- to late-stage controlled degradation of implanted hydrogels is critical for effective TBI treatment and promotion of damaged brain tissue regeneration. Therefore, we investigated the relationship between degradation and the mechanical properties of the LMSA hydrogel. In vitro degradation studies showed that LMSA hydrogels immersed in ACSF or glutathione (GSH)–containing phosphate-buffered saline (PBS) achieved nearly complete degradation within 28 days (fig. S7), meeting the requirements for TBI therapy. Subsequently, we monitored the evolution of mechanical strength at different time points during degradation. Results revealed that during the early degradation phase (0 to 7 days), the moduli of LMSA-0.25 and LMSA-0.3 remained consistently within the range of native brain tissue, indicating their capacity to provide effective mechanical support during the initial postimplantation stage. As time prolonged, the hydrogel underwent gradual degradation, resulting in decreased modulus, which satisfies the requirement for controlled degradation to accommodate progressive tissue ingrowth during brain injury repair (figs. S8 and S9). To more precisely validate the in vivo degradability of LMSA, we further investigated its degradation behavior through subcutaneous implantation. As shown in fig. S10A, the LMSA hydrogel gradually degraded in vivo and achieved complete degradation within 28 days, attributed to the abundant GSH in the physiological environment that cleaves the disulfide bonds in the PolyLA backbone, reducing it into oligomers or small molecules (fig. S11). These degradation products can be eliminated via renal excretion in urine or biliary excretion through the gallbladder (*36*–*38*). Subcutaneous tissues in contact with the material were collected at different time points for hematoxylin and eosin (H&E) and Masson staining analysis (fig. S10, B and C). The results revealed that LMSA did not induce notable chronic inflammatory responses or other adverse tissue reactions, confirming its excellent tissue compatibility.

While adhesion is not an indispensable requirement for TBI treatment, it can serve as a beneficial supporting function to facilitate efficient TBI therapy. Although it does not notably contribute to biological regulation, it is beneficial for sealing irregular brain defects, optimizing the electrode-tissue interface, reducing interfacial impedance, and maintaining stable ES delivery and ECoG signal acquisition throughout the experimental process. Our team's previous research (*26*, *33*, *39*–*42*) has demonstrated that PolyLA-based materials achieve adhesion by forming multiple hydrogen bonds and electrostatic interactions between the abundant adhesive carboxyl groups on the PolyLA backbone and the tissue. Consequently, we evaluated the tissue adhesion properties of the LMSA hydrogels. As shown in Fig. 3D, the LMSA hydrogel exhibited strong adhesion to various wet soft tissues, including brain tissue. In a tilted-plane adhesion test, fresh rat brain tissue remained stably adhered to the hydrogel

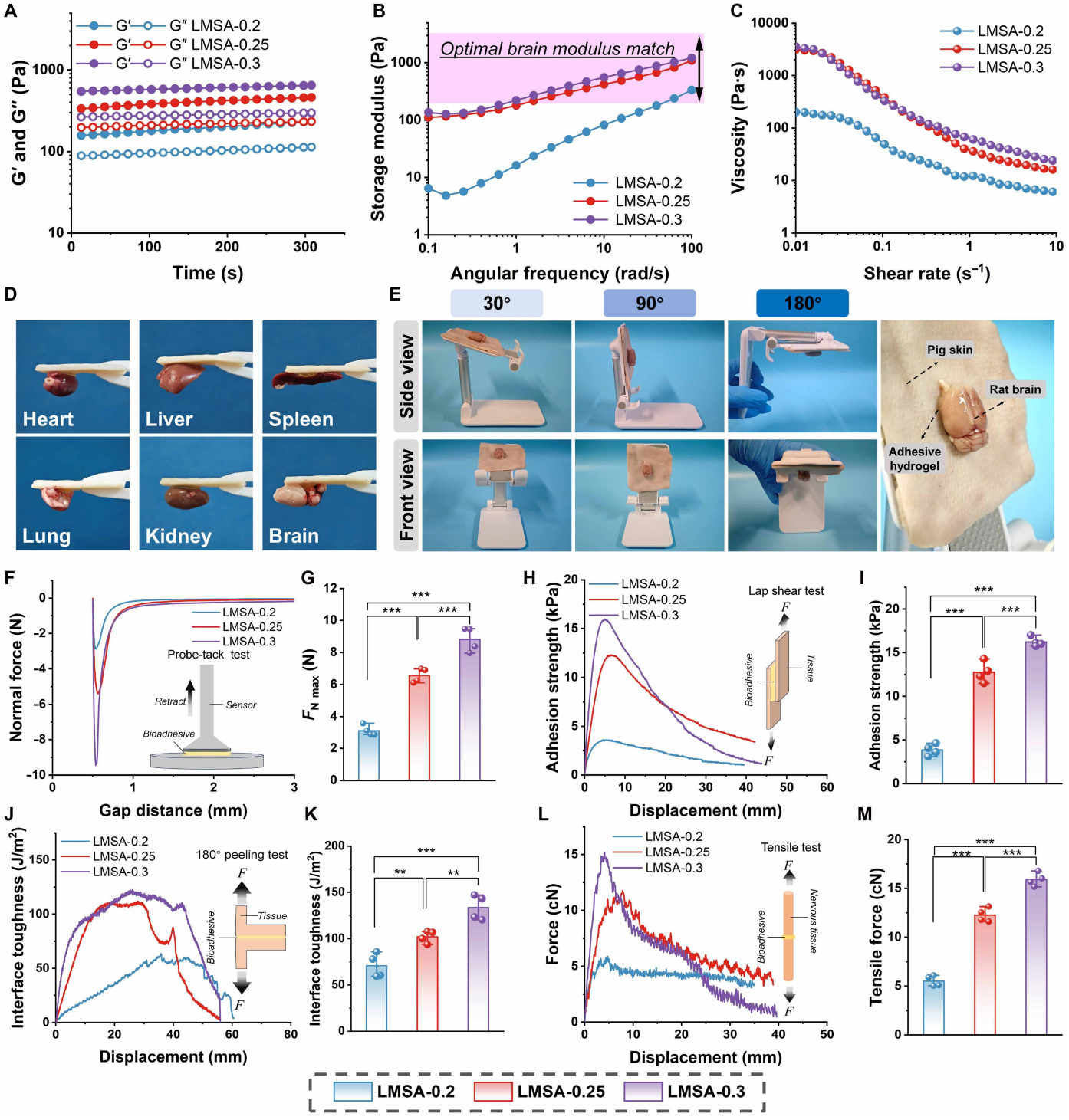

Fig. 3. Mechanical and adhesive properties of LMSA hydrogels. (**A**) Time sweep of LMSA hydrogels with different compositions. (**B**) Angular frequency sweep of LMSA hydrogels with different compositions. (**C**) Shear rate–viscosity curve of LMSA hydrogels with different compositions. (**D**) Adhesion ability of LMSA-0.25 to various wet tissues. (**E**) Evaluation of LMSA hydrogel adhesion effect using the tilted plane method. (**F** and **G**) Probe-tack test curves and maximum adhesion force of LMSA hydrogels with different compositions. (**H** and **I**) Lap shear test curves and adhesion strength of LMSA hydrogels with different compositions on fresh porcine skin. (**J** and **K**) 180° peeling test curves and interface toughness of LMSA hydrogels with different compositions on fresh porcine skin. (**L** and **M**) Tensile test curves and tensile force of LMSA hydrogels with different compositions on fresh porcine sciatic nerve. ($n = 4$, $^{**}P < 0.01$, and $^{***}P < 0.001$)

surface without detachment, even at a 180° tilt (Fig. 3E). Subsequently, we quantitatively characterized the adhesion properties of LMSA hydrogels using four models: a probe-tack adhesion test, a lap shear test, a 180° peel test, and a tensile test. Adhesion probe tests revealed that the debonding mode of the LMSA hydrogel is cohesive failure (fig. S12), and the detachment force (Fig. 3, F and G) and adhesion work (fig. S13) significantly increase with higher LA/Met content. In addition, lap-shear tests were performed using fresh porcine skin to evaluate the shear resistance of LMSA hydrogels to tissue. The results show that adhesion strength increases with increasing LA/Met content, and LMSA-0.3 exhibited the highest adhesion strength of 16.21 ± 0.55 kPa. This may be because LMSA-0.3 exhibits the strongest bulk strength (Fig. 3, H and I). Next, the interfacial toughness of the LMSA hydrogels to tissue was assessed using a 180° peeling test (Fig. 3J). Consistent with the above results, LMSA-0.3 exhibited the strongest interfacial toughness, at 133.42 ± 13.53 J/m^2 (Fig. 3K). To evaluate the adhesion performance of the LMSA hydrogel to neural tissue, tensile tests were conducted on its adhesion to porcine sciatic nerve. The results showed that all hydrogel formulations adhered effectively to neural tissue and could withstand a certain degree of strain (fig. S14). The measured adhesion force for LMSA-0.2, LMSA-0.25, and LMSA-0.3 was 5.51 ± 0.54, 12.26 ± 0.71, and 15.90 ± 0.68 cN, respectively (Fig. 3, L and M), which is crucial for mitigating the elastic recoil of the nerve epineurium during the repair of nerve transection. In summary, the LMSA hydrogel demonstrates notable potential as an adhesive material for neural tissue repair. Furthermore, we evaluated the wet-resistant adhesion of the LMSA hydrogel. Results showed that after 48 hours of immersion in ACSF or GSH-containing PBS, LMSA-0.25 still exhibited an adhesion work of 1.01 ± 0.10 or 0.97 ± 0.06 J/m^2 (figs. S15 and S16), demonstrating reliable wet-resistant adhesion sufficient to maintain durable electrode-tissue fixation.

In vitro bioactivity of LMSA hydrogels

Previous studies have demonstrated that LA has potent antioxidant, anti-inflammatory, and antibacterial properties and can treat neuropathy by enhancing endogenous GSH levels, reducing lipid peroxidation, improving mitochondrial and vascular endothelial function, inhibiting protein glycation, and increasing nerve conduction velocity (*27*, *40*, *43*). Meanwhile, Met has been shown to promote the recruitment of endogenous NSCs and participate in the repair of damaged brain structures. Therefore, the localized codelivery of LA and Met directly to the TBI site is a crucial strategy for harnessing their synergistic potential in neural repair. In this study, the introduction of Met promotes LA release by inducing partial deprotonation of LA due to Met's basic nature. To evaluate LA release behavior, the intensity of the characteristic five-membered ring peak at 330 nm in the UV-visible (UV-Vis) spectra was monitored. The release rate of LA monomers from LMSA hydrogels was assessed in ACSF. As shown in fig. S17 (A to C), the absorbance peak intensity at 330 nm increased gradually over time. We then quantified LA release kinetics, showing rapid release in the first 48 hours and slow, sustained release over the next 10 days (fig. S17D). This biphasic pattern is likely attributable to the initial release of more hydrophilic LA salt structures, followed by the gradual degradation of the hydrophobic PolyLA backbone, which liberates the remaining LA. An identical trend was observed for Met release, which was quantified using high-performance liquid chromatography (fig. S18). In summary, the in vitro release studies revealed that LA and Met exhibited a predominantly early-stage release (within 48 hours). This rapid release is therapeutically advantageous, enabling timely intervention following local administration of LMSA hydrogels (fig. S19). It allows for addressing the acute inflammatory phase (days 1 to 3), mitigating long-term pathological sequelae from delayed treatment, and promoting the recruitment of endogenous NSCs. The sustained LA release over 3 to 7 days effectively targets the chronic TBI phase (days to weeks), modulating inflammation and promoting tissue repair.

Excessive reactive oxygen species production at the TBI site damages proteins, lipids, and nucleic acids, thereby irreversibly exacerbating brain injury. Therefore, we first evaluated the in vitro antioxidant capacity of LMSA hydrogels. Macroscopic images of the 1,1-diphenyl-2-picrylhydrazyl (DPPH) free radical scavenging assay showed that the PBS control group remained blue-violet after 48 hours, whereas all LMSA hydrogels turned light yellow (fig. S20A). Quantitative analysis via UV-Vis spectroscopy revealed that after 48 hours of cocultivation, the DPPH scavenging efficiencies of LMSA-0.2, LMSA-0.25, and LMSA-0.3 were 77.6 ± 1.2, 81.7 ± 0.7, and 82.7 ± 0.7%, respectively, showing a positive correlation with the LA release rate (fig. S20, B to E). The 2,2-azino-bis(3-ethylbenzothiazoline-6-sulfonic acid) diammonium salt (ABTS) radical scavenging assay demonstrated that the hydrogels achieved nearly 100% scavenging efficiency after 6 hours of cocultivation, as indicated by the complete fading of the blue-green color to colorless (fig. S21). In addition, the hydrogels exhibited hydroxyl radical (·OH)–scavenging capacities exceeding 85% within 0.5 hours (fig. S22). These results collectively indicate that LMSA hydrogels has satisfactory antioxidant capacity.

Electrical conductivity properties of LMSA hydrogels

Sufficient electrical conductivity of the hydrogel is a prerequisite for applying exogenous ES and recording electrical signals. The LMSA hydrogel achieves ionic conductivity by leveraging H^+ ions from carboxyl groups as the primary charge carriers (*39*, *40*). The dynamic hydrogen/ionic bonding network between guanidyl and carboxylate groups creates an efficient proton-hopping channel, a process further facilitated by water molecules (Fig. 4A). As shown in Fig. 4B, the electrical conductivity of the LMSA hydrogel increased with the solid content of LA and Met. Notably, LMSA hydrogel exhibited a conductivity ranging from 0.3 to 0.7 S m^{-1}, which matches that of physiological nervous tissues (0.03 to 0.6 S m^{-1}) (*44*). A systematic comparison with previously reported hydrogels for TBI treatment reveals that LMSA-0.25 exhibits mechanical strength and electrical conductivity matching those of neural tissue, along with an adhesion-assisting effect (Fig. 4C and table S1). On the basis of this balanced performance, LMSA-0.25 was chosen as the primary candidate for all further testing and in vivo experiments. ES presents a promising approach for promoting the effective differentiation of NSCs into neurons. However, conventional methods often require high operating voltages, which can induce local water electrolysis and hydrogen evolution at the electrode-tissue interface, severely impairing tissue repair and regeneration. Therefore, developing a safer ES modality is essential. In this work, we designed a flexible stimulating electrode capable of delivering biphasic pulsed current to the tissue (fig. S23). This stimulation mode prevents charge accumulation and associated tissue damage inherent to unidirectional stimulation. Furthermore, by integrating this flexible electrode with the adhesive LMSA hydrogel, we anticipate further enhancing electrode compatibility, ES safety, and signal transmission efficiency. Using an electrochemical workstation, we systematically compared the impedance, charge storage

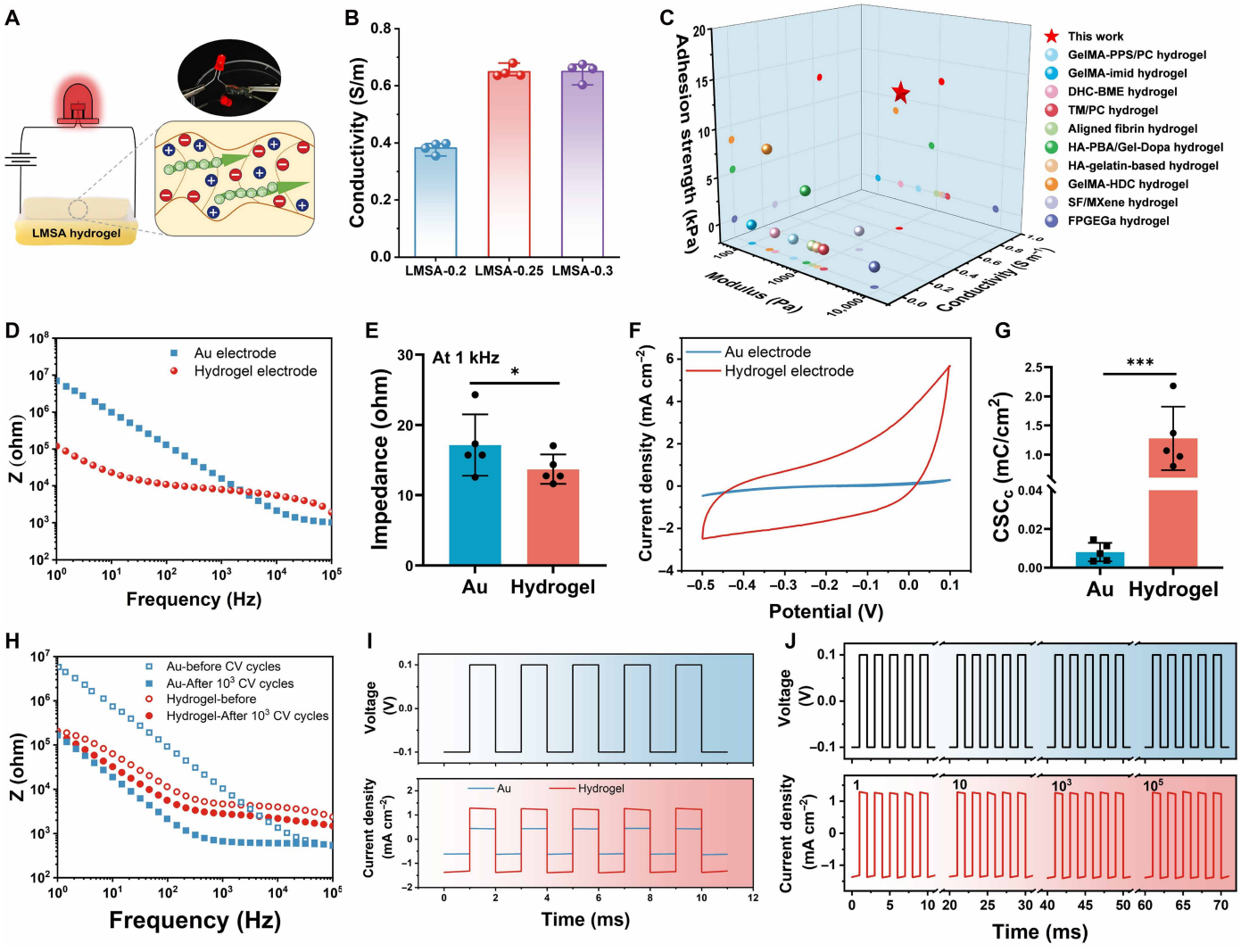

Fig. 4. Electrical conductivity properties of LMSA hydrogels. (**A**) Diagram of the ionic conduction mechanism of LMSA hydrogel. (**B**) The conductivity of LMSA hydrogels with different compositions ($n = 4$). (**C**) The figure compares the modulus, conductivity, and adhesion strength of the LMSA hydrogel with those of previously reported hydrogels for TBI treatment. (**D**) Impedance spectra of Au and hydrogel electrodes across the frequency range. (**E**) Impedance magnitude comparison at 1 kHz ($n = 5$). (**F**) CV scans from −0.5 to 0.1 V. (**G**) CSC quantification ($n = 5$). (**H**) Postcycling impedance spectra after 1000 CV cycles. (**I**) Charge density transients under ±0.1-V pulsed stimulation. (**J**) Charge injection capacity retention during cyclic testing. (*$P < 0.05$ and ***$P < 0.001$)

capacity (CSC), and charge-injection performance of our hydrogel-integrated electrodes with those of conventional Au electrodes. For neural interfaces, low impedance and high CSC are critical for performance as they reduce signal attenuation and noise, improve detection sensitivity and signal fidelity, suppress electrochemical polarization, maintain interfacial pH stability, minimize tissue damage, and enhance long-term stability. Our hydrogel-integrated electrodes exhibited significantly lower impedance than Au electrodes across the low-frequency to physiologically relevant range (up to ~1 kHz; Fig. 4, D and E). This improved impedance profile contributes to a higher signal-to-noise ratio, enabling more accurate recording of local field potentials (LFPs) (*45*). Furthermore, the hydrogel-integrated electrodes demonstrated a CSC greater than that of the Au electrodes (Fig. 4, F and G). This enhanced CSC facilitates rapid charge delivery and high-frequency pulse output, both critical for dynamic neural signaling, thereby improving stimulation accuracy. To assess operational durability, we performed cyclic voltammetry (CV) over multiple charge-discharge cycles. The hydrogel-integrated electrodes showed negligible impedance change after 1000 cycles, indicating superior cycling stability compared to Au electrodes (Fig. 4H and fig. S24). We also evaluated charge-injection performance, a key metric for neural modulation. At a fixed voltage (±0.1 V, 1 ms), the hydrogel-integrated electrodes achieved a higher current density than the Au electrodes (Fig. 4I), indicating that lower operating voltages can yield equivalent stimulation. This characteristic helps minimize undesirable side reactions, maintain interfacial pH stability, and improve the biosafety of ES (*46*). Long-term charge injection tests further confirmed that the hydrogel-integrated electrodes maintain stable performance, supporting their suitability for chronic neural interface applications (Fig. 4J).

Cytocompatibility and stimulating differentiation on NSCs of the LMSA hydrogel + ES

Cytocompatibility is a fundamental requirement for in vivo applications of biomaterials. To evaluate the biocompatibility of LMSA hydrogel, systematic in vitro experiments were conducted. CCK-8 assays and live/dead cell staining indicated that the hydrogel showed no significant cytotoxicity toward both PC12 (a model of neuroendocrine cells) and NSCs, even at 1 mg/ml (Fig. 5, A and B). It has been reported that Met can promote the in situ recruitment of NSCs (*24*). On the basis of the degradation and bioactive molecule release properties of the LMSA hydrogel, we next investigated the chemoattractive effect of LMSA degradation products on NSCs using a Transwell migration assay. In this setup, the lower chamber contained the degradation product of LMSA hydrogel to simulate the drug release environment at the injury site, while the upper chamber was seeded with NSCs to mimic stem cells in the surrounding tissue. Crystal violet staining revealed significantly more NSCs migrating from the upper chamber in the hydrogel group than in the control group, indicating the potential to recruit endogenous stem cells of LMSA (fig. S25).

The ES parameters were selected on the basis of previous studies (*45*, *47*), using a biphasic charge–balanced rectangular current pulse (130 Hz, 50 μA, and 1-ms pulse width) delivered to the right sensorimotor cortex of rats since high-frequency stimulation (130 to 180 Hz) is believed to be more conducive to promoting the treatment, while a 50-μA current is a commonly used and safe starting value for cortical microstimulation (*48*). Biphasic charge–balanced pulses effectively suppress irreversible Faradaic reactions, pH drift, and hydrolysis, thereby enhancing the reversibility and long-term stability of the stimulation (*49*). In addition, the intermittent (duty cycle) stimulation pattern reduces the time-averaged charge injection and thermal load while enabling depolarization and recovery of the electrode-tissue interface during the off periods. Consequently, the 50 μA, 130-Hz pulsed current was adopted as the standard ES parameter for both in vitro and in vivo studies. Moreover, PC12 viability was not affected by biphasic stimulation across 20 to 100 μA, indicating good cytocompatibility over a broad amplitude range (fig. S26). In addition, cell compatibility assays have shown that the hydrogel combined with ES significantly promotes PC12 cell proliferation, once again demonstrating the synergistic effect of the combined approach (fig. S27). Meanwhile, we used a scratch assay to evaluate the potential of the LMSA hydrogel + ES to facilitate the recruitment of endogenous NSCs in vitro. As shown in Fig. 5E, at the 8-hour time point, NSCs in all groups migrated toward the center of the scratch. Among them, the hydrogel + ES group exhibited a significantly higher cell migration area (46.66 ± 4.53%) compared to the control group (22.45 ± 5.17%), the hydrogel group (39.43 ± 7.86%), and the ES group (37.65 ± 2.40%) (Fig. 5F). These results indicate that the synergistic effect of LMSA hydrogel and ES significantly enhances the migratory capacity of NSCs, suggesting its potential to promote the recruitment of endogenous NSCs in vivo. This is of great significance for neuronal replenishment and neuroregeneration following TBI. The combined efficacy of the ES and hydrogel system was evaluated using NSCs. NSCs were seeded in 24-well plates and subjected to different interventions. After a 7-day treatment, the differentiated cells were subjected to immunofluorescence staining. Nestin served as a marker for NSCs, and βIII-tubulin (Tuj-1) was used to identify neuronal cells (Fig. 5G) (*7*, *20*). The number of Nestin-positive and Tuj-1–positive cells was quantified (*50*). The proportion of Tuj-1–positive cells within the Nestin-positive cell population was then calculated, as shown in Fig. 5H. ES significantly enhanced NSC differentiation into neuronal cells, achieving a differentiation rate of ~60%, compared to ~45% in the control group. Moreover, when combined with the hydrogel, the neuronal differentiation rate was further increased to nearly 80%. These results collectively indicate that the combination of ES and hydrogel can significantly promote neuronal differentiation (Fig. 5D). This promising outcome suggests a potential therapeutic strategy for TBI repair.

NSCs recruitment and differentiation properties of LMSA hydrogel + ES in vivo

To further evaluate the in vivo efficacy of LMSA hydrogel + ES in brain tissue regeneration and neural repair, we established a rat model of substantial brain defect following acute TBI using the controlled cortical impact (CCI) method. Before in vivo studies, we first evaluated the hemocompatibility of the LMSA hydrogel, as it is a critical parameter for assessing biocompatibility. The results showed that the hemolysis rates for all tested concentrations of the LMSA hydrogel were below 5%, indicating its good hemocompatibility (fig. S28). The hydrogels were subsequently injected into the brain lesion site, followed by electrode implantation for subsequent ES therapy (Fig. 6, A and B). At designated intervals, ES therapy was applied, and electrical signals were recorded (Fig. 6C and fig. S29), along with the associated behavioral evaluations. As shown in Fig. 6D, the ES was delivered daily for five consecutive days, with each session lasting 20 min. Representative biphasic current stimulation waveforms recorded by an oscilloscope are presented in Fig. 6E. This combined strategy facilitated an integrated platform for TBI treatment and neurological recovery monitoring. The detailed experimental timeline is illustrated in fig. S30.

Next, we investigated the in situ recruitment and differentiation effects of LMSA combined with ES on endogenous NSCs in vivo. We performed immunofluorescence staining to evaluate the expression of Nestin, a specific marker of NSCs, at 7 days postinjury (dpi), to assess the impact of different treatment strategies on NSC recruitment. As shown in Fig. 6 (F and H), the TBI + hydrogel (15.3 ± 1.13%) and TBI + ES (3.9 ± 0.86%) groups showed increased signals over untreated TBI (1.7 ± 0.08%). The combined TBI + hydrogel + ES group exhibited the strongest $Nestin^+$ staining (25.2 ± 2.25%), a 14.8-fold increase. These results demonstrate that LA-mediated microenvironment remodeling and Met synergistically recruit endogenous NSCs, with ES further amplifying this effect. Given that NSCs can differentiate into various cell types, including beneficial neurons and oligodendrocytes, as well as detrimental astrocytes, we further analyzed their differentiation patterns across groups at 14 dpi. Immunofluorescence staining was used to assess the expression of βIII-tubulin (Tuj-1, a marker of immature neurons), neuronal nuclei (NeuN, a marker of mature neurons), myelin basic protein (MBP, a marker of oligodendrocytes), and glial fibrillary acidic protein (GFAP, a marker of astrocytes). As shown in Fig. 6 (G and I) and figs. S31 to 33, compared to the untreated TBI group, both the TBI + hydrogel group and the TBI + ES group exhibited significantly up-regulated expression of Tuj-1, NeuN, and MBP, while GFAP expression was significantly reduced. This differentiation-regulating effect was further enhanced in the TBI + hydrogel + ES group, which exhibited 11.3-, 4.1-, and 14.6-fold increases in Tuj-1, NeuN, and MBP expression, respectively, while $GFAP^+$ expression dropped to only 31% of control levels. This confirms that the combined treatment of hydrogel and ES promotes

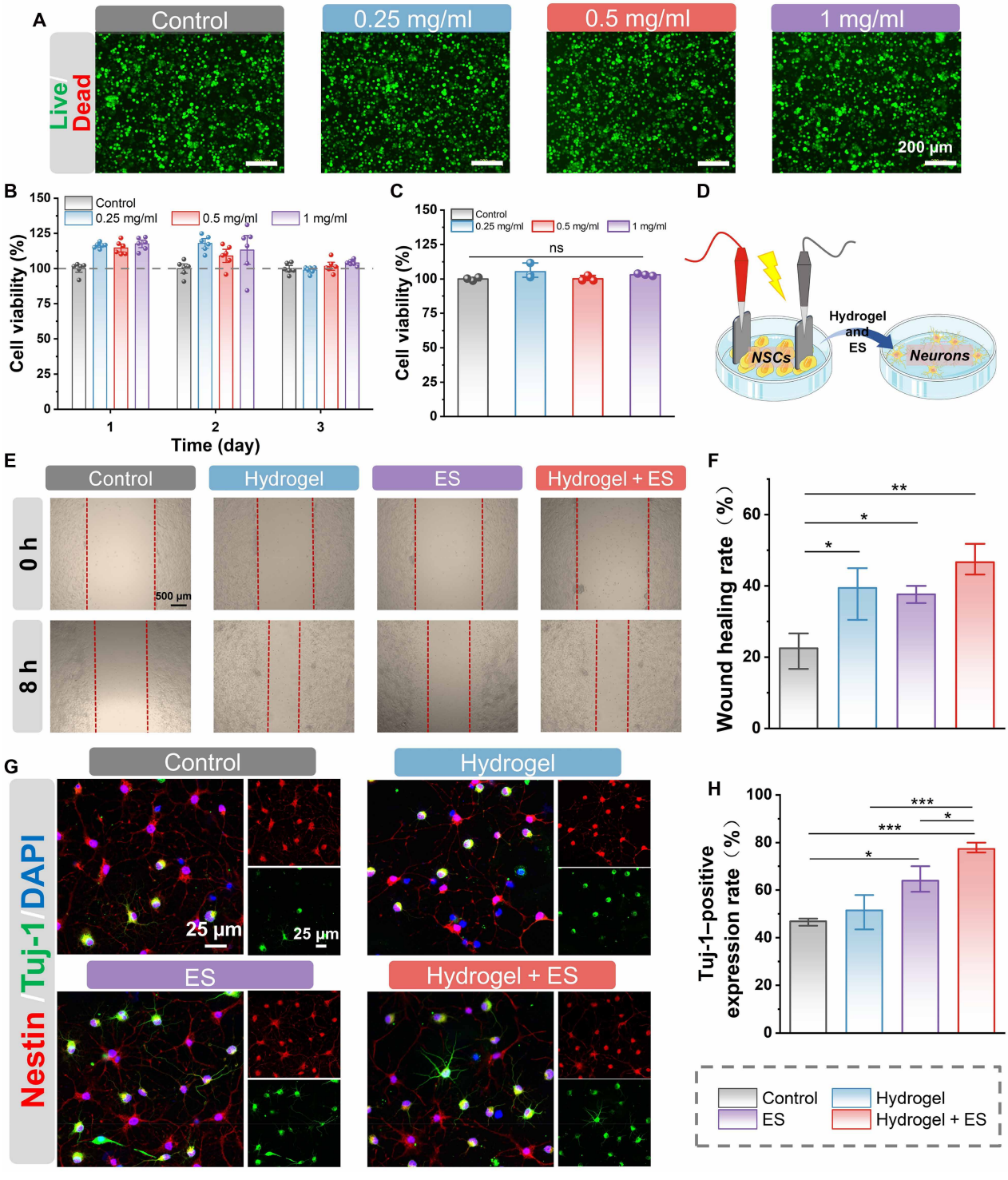

Fig. 5. Cytocompatibility and NSCs differentiation-promoting activity of LMSA hydrogel + ES. (**A**) Live-dead staining characterizes the cytocompatibility of LMSA-0.25 hydrogel to PC12 cells. (**B**) CCK-8 assay for detecting cell viability of the coculture of PC12 cells with LMSA-0.25 hydrogel ($n = 6$). (**C**) CCK-8 assay for detecting cell viability of the coculture of NCSs with LMSA-0.25 hydrogel ($n = 3$). (**D**) Schematic diagram showing that the combined intervention with ES and hydrogel notably promotes neuronal differentiation. (**E**) NSCs scratch assay results for 8 h (hours). (**F**) Quantitative analysis of the wound closure percentage in the scratch assay ($n = 3$). (**G**) Nestin and Tuj-1 immunofluorescence images of NSCs. Nestin was labeled in red, while Tuj-1 was labeled in green. Nuclei were labeled with 4′,6-diamidino-2-phenylindole (DAPI) in blue. (**H**) Ratios of Tuj-1–positive expression based on immunofluorescence staining results ($n = 3$). (*$P < 0.05$, **$P < 0.01$, and ***$P < 0.001$).

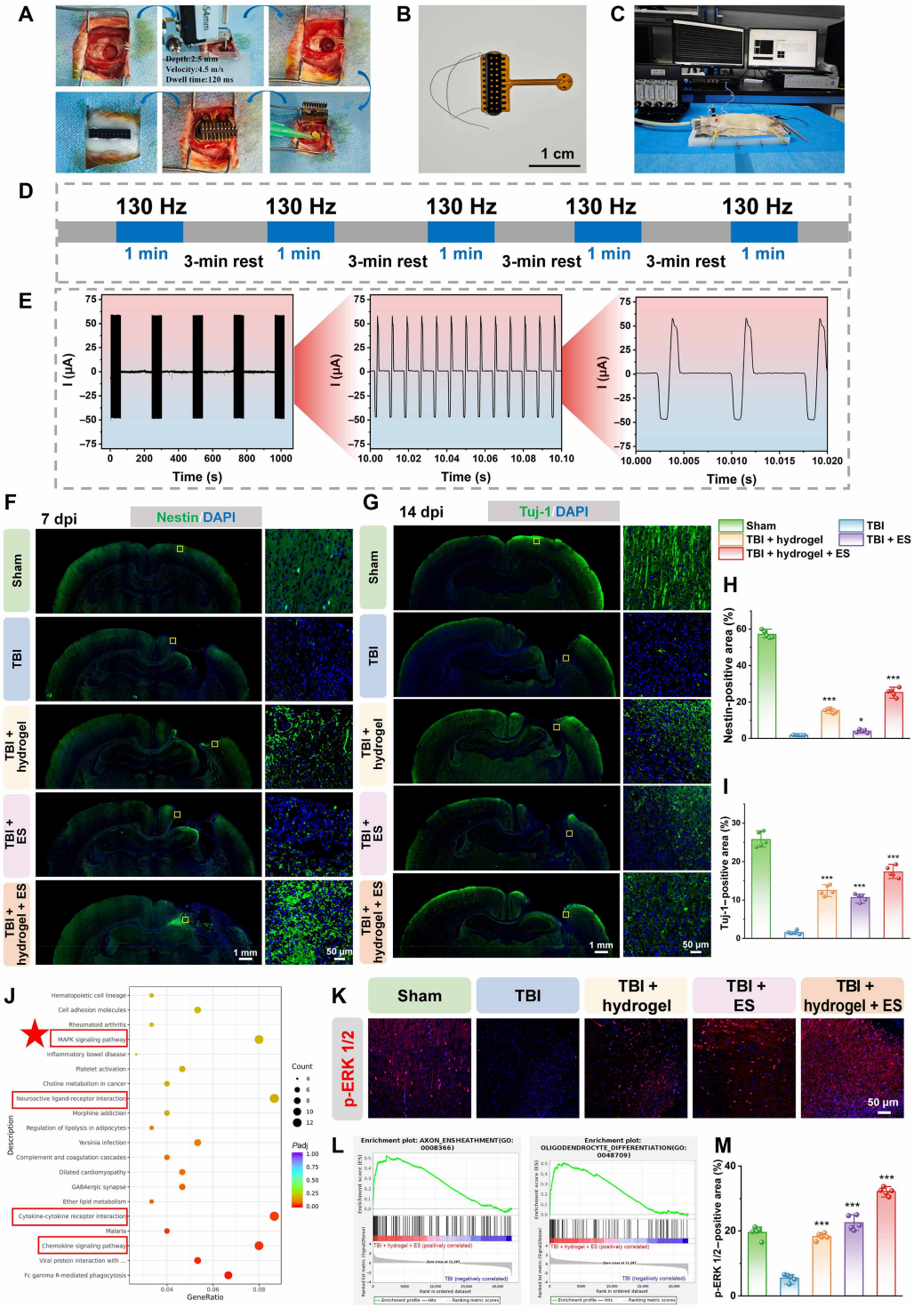

Fig. 6. LMSA hydrogel + ES promotes the recruitment and differentiation of endogenous NSCs in the lesions. (**A**) Photographs show the schematic illustration of the surgical procedures for establishing the TBI model in rats, as well as the hydrogel injection and electrode implantation. (**B**) Digital photograph of implanted electrodes. (**C**) Photographs present experimental images of rats during the process of recording electrical signals. (**D**) A typical ES session lasts 20 min. (**E**) ES waveform recorded by an oscilloscope. (**F**) Typical immunofluorescence staining pictures of Nestin (green) to investigate the recruitment of endogenous NSCs in the injured area at 7 dpi. (**G**) Typical immunofluorescence staining pictures of Tuj-1 (green) to assess the differentiation of NSCs into neurons in the lesion at 14 dpi. (**H**) Quantification of Nestin-positive area per field ($n = 5$). (**I**) Quantification of Tuj-1–positive area per field ($n = 5$). (**J**) Kyoto Encyclopedia of Genes and Genomes pathway enrichment bubble plot for differentially expressed genes between the TBI group and the TBI + hydrogel + ES group. (**K**) Typical immunofluorescence staining pictures of p-ERK1/2 (red) in the lesion at 7 dpi. (**L**) Gene Set Enrichment Analysis results of the TBI group and the TBI + hydrogel + ES group. (**M**) Quantification of p-ERK1/2–positive area per field ($n = 5$). The yellow square boxes indicate the close-up areas. (*$P < 0.05$ and ***$P < 0.001$ compared to the TBI group)

neuronal differentiation and maturation of recruited NSCs at the injury site and inhibits their differentiation into astrocytes. Furthermore, Nissl staining results showed that at 28 dpi (fig. S34), the TBI + hydrogel + ES group exhibited higher neuronal density and activity than the untreated TBI group and the other single-therapy groups. Together, our data indicate that the combined intervention of hydrogel and ES synergistically recruits endogenous NSCs and favorably steers their fate commitment towards neurons and oligodendrocytes, accelerating functional integration, while minimizing glial scar formation by suppressing astrocytic differentiation. These findings highlight the therapeutic potential of this combinatorial strategy for TBI repair.

To further investigate the molecular mechanisms by which the hydrogel + ES promotes NSC recruitment post-TBI, we conducted RNA sequencing to assess the impact of combined LMSA hydrogel and ES treatment on gene expression. Sample quality was validated using Pearson correlation and principal components analysis (fig. S35), with results indicating high reproducibility among the samples ($R^2 \geq 0.8$, $n = 3$). As shown in fig. S36, Venn diagram analysis revealed 14,605 overlapping genes between the two groups, with 880 unique differentially expressed genes in the TBI + hydrogel + ES group and 624 in the untreated TBI model group. Volcano plots and heatmaps showed that, compared to the untreated TBI group, the TBI + hydrogel + ES group exhibited 194 up-regulated and 125 down-regulated genes. In addition, the Gene Set Enrichment Analysis revealed that in the TBI + hydrogel + ES group (Fig. 6L and fig. S37), gene sets related to glial cell differentiation, oligodendrocyte generation, and neuronal myelination were notably enriched, suggesting that this treatment strategy positively modulates myelin regeneration, which is essential for neural function recovery. As shown in fig. S38, Gene Ontology analysis revealed that differentially expressed genes were primarily enriched in biological processes, including neuronal sheath formation, axonal myelination, myelinogenesis, glial and oligodendrocyte differentiation, and postsynaptic density. As shown in Fig. 6J, Kyoto Encyclopedia of Genes and Genomes pathway enrichment analysis further indicated that these differentially expressed genes were mainly involved in pathways including "cytokine-cytokine receptor interaction," "neuroactive ligand-receptor interaction," "chemokine signaling pathway," and "mitogen-activated protein kinase (MAPK) signaling pathway." Among these, the MAPK pathway is activated under stimulation and mediates extracellular signals to the nucleus via the phosphorylation of ERK1/2, thereby regulating processes such as cell proliferation, differentiation, and migration. The cytokine-receptor interaction pathway plays a crucial role in regulating inflammatory responses, cell growth, differentiation, apoptosis, and angiogenesis. The chemokine signaling pathway plays a crucial role in tissue regeneration, development, and angiogenesis, guiding stem cell migration and providing maturation signals that facilitate tissue repair and regeneration after injury. Further analysis of pathways involved in neuronal differentiation induced by the hydrogel and ES revealed that the expression of phosphorylated ERK1/2 (p-ERK1/2) was significantly higher in the TBI + hydrogel + ES group compared to the untreated TBI group (Fig. 6, K and M), indicating that this combined treatment effectively activates the MAPK signaling pathway to promote neuronal differentiation. These findings are consistent with previous studies (*20*, *51*), which confirm the critical role of ES in neuronal differentiation and further support the therapeutic potential of the hydrogel combined with ES for TBI repair.

LMSA hydrogel + ES promotes TBI brain structural reconstruction

Aberrant activation of microglia and astrocytes after TBI drives sustained neuroinflammation, releasing proinflammatory mediators that exacerbate neuronal injury and trigger secondary pathological cascades. Given the potential anti-inflammatory properties of LA, this study systematically evaluated the efficacy of various treatment strategies in mitigating post-TBI neuroinflammation. By assessing the expression levels of GFAP and Iba-1 (markers of glial activation), as well as CD86 (a marker of M1 polarization) and CD206 (a marker of M2 polarization), we found that glial activation was significantly increased in the untreated TBI group at 7 dpi (Fig. 7, A, C, and D). In contrast, other groups exhibited markedly reduced glial activation, with the most pronounced effect observed in the TBI + hydrogel + ES group. Moreover, compared to the TBI group, both the TBI + hydrogel group and the TBI + ES group markedly attenuated the proinflammatory M1 phenotype and enhanced the anti-inflammatory M2 state (figs. S39 and S40). The TBI + hydrogel + ES group demonstrated the most significant regulatory effect. These findings suggest that the combined treatment strategy mitigates TBI-induced neuroinflammation by inhibiting glial overactivation and modulating glial polarization.

Following TBI, abnormal astrocyte activation and excessive proliferation are common pathological responses that lead to the formation of dense glial scars at the injury site. These glial scars not only restrict brain tissue regeneration but also act as physical barriers that impede axonal regrowth and neural network reconstruction, thereby hindering functional recovery. Next, the formation of glial scars was evaluated across the treatment groups. Double immunofluorescence staining for GFAP and Tuj-1, in conjunction with Masson's trichrome staining, was used to observe the distribution and density of glial fibers. As shown in fig. S41, the untreated TBI group exhibited high GFAP expression at 28 dpi, accompanied by widespread glial scarring. In contrast, both the TBI + hydrogel group and the TBI + ES group showed significantly reduced GFAP-positive signals, indicating that these two treatment strategies can suppress glial scar formation. Notably, the TBI + hydrogel + ES group showed nearly undetectable GFAP-positive signals at 28 dpi, demonstrating a significant synergistic effect in suppressing astrocytic overproliferation. As shown in Fig. 7G and fig. S42, Masson's trichrome staining further revealed that the TBI + hydrogel + ES group showed the most prominent scar suppression, with a collagen rate of 29.65 ± 2.20%, compared to 58.50 ± 3.23% in the untreated TBI group. The combined treatment reduced the collagen area by nearly twofold.

Angiogenesis plays a crucial role in tissue regeneration. To evaluate vascular integrity at the lesion site, we performed costaining for CD31 (an endothelial cell marker) and α-SMA (a marker for vascular smooth muscle cells and pericytes). As shown in figs. S43 and S44, the untreated TBI group exhibited minimal CD31 and α-SMA staining at the injury site, indicating a significant impairment in angiogenic capacity. In contrast, other groups showed varying degrees of increased expression of vascular markers. Among these, the TBI + hydrogel + ES group exhibited the most pronounced enhancement of CD31 and α-SMA signals at both 14 and 28 dpi, with a clear increase in mature vascular structures. These findings suggest that the combined application of hydrogel and ES significantly enhances post-TBI angiogenic capacity, thereby providing sufficient oxygen and nutrient supply for neuronal proliferation, migration, and neural circuit reconstruction, thereby improving the local microenvironment and promoting functional recovery.

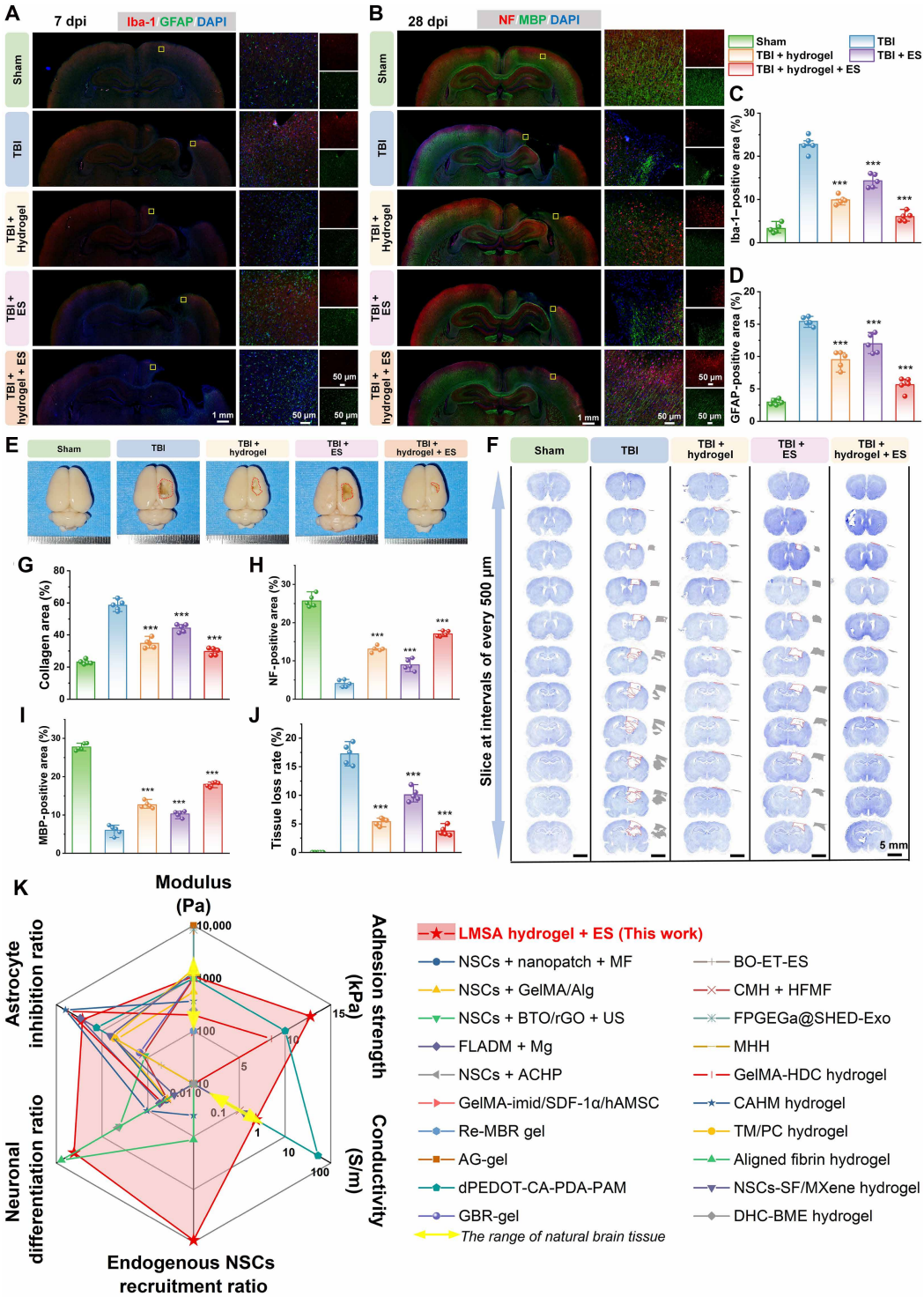

Fig. 7. LMSA hydrogel + ES reshapes the microenvironment and promotes brain tissue structural remodeling. (**A**) Representative double immunofluorescence staining pictures of Iba-1 (red) and GFAP (green) to investigate suppression of neuroinflammation at the lesion site at 7 dpi. (**B**) Representative double immunofluorescence staining pictures of NF (red) and MBP (green) to evaluate the axonal regeneration and remyelination at the lesion site at 28 dpi. (**C** and **D**) Quantification of Iba-1– and GFAP-positive area per field ($n = 5$). (**E**) Digital photographs of rat brain tissue at 28 dpi. The red dashed line indicates the boundary of tissue loss. (**F**) Representative images of Nissl staining at 28 dpi across all groups. The red dashed line indicates the boundary of tissue loss. (**G**) Quantification of collagen area per field ($n = 5$). (**H** and **I**) Quantification of NF- and MBP-positive area per field ($n = 5$). (**J**) Quantification of tissue loss rate at 28 dpi ($n = 5$). (**K**) A radar chart comparing the performance and repair effect of LMSA hydrogel + ES with the recently reported TBI treatment methods. The yellow square boxes indicate the close-up areas. (***$P < 0.001$ compared to the TBI group)

In addition, structural damage to key neural elements—including axons, myelin, and synapses—is a hallmark of TBI that persists long-term, constituting the core pathological substrate for chronic neurological dysfunction. Although the restoration of these structures is essential for recovery, the endogenous potential for axonal regeneration is poor, and spontaneous repair of myelin and synapses remains exceedingly limited, thereby severely impeding functional restoration. To assess neural regeneration across treatment groups, we performed dual immunofluorescence staining for neurofilament (NF, marking axons and mature neural fibers) and MBP (labeling myelin sheaths). As depicted in Fig. 7 (B, H, and I), immunohistochemical analysis at 28 dpi revealed negligible NF and MBP signals in the lesion area of the TBI group, indicating severely impaired axonal regeneration and remyelination. While individual treatments moderately improved this outcome, the combined strategy led to a markedly augmented presence of NF axons and MBP myelin, providing clear evidence of a synergistic interaction in reconstructing the damaged neuroarchitecture. Luxol fast blue (LFB) staining further confirmed that the TBI + hydrogel + ES group exhibited the most notable myelin regeneration (fig. S45). Growth-associated protein (GAP43) is a key marker for axonal sprouting and the formation of nascent synapses. The highest expression of GAP43 was observed in the TBI + hydrogel + ES group (fig. S46), suggesting that the combined hydrogel and ES strategy effectively promotes synaptic regeneration.

To further evaluate structural repair, rat brains were harvested at 28 dpi. Macroscopic examination revealed pronounced tissue defects in the TBI group, which were mitigated by either hydrogel or ES treatment. Notably, the combined TBI + hydrogel + ES group exhibited the most intact tissue architecture (Fig. 7E), a finding corroborated by Nissl staining (Fig. 7F). H&E staining further confirmed these observations (fig. S47): While the TBI group displayed large cavitated lesions, both monotherapies reduced cavity size and improved tissue integrity. The combined treatment yielded the best outcome, characterized by minimal lesion area and densest cellular organization. These results confirm the synergistic potential of the LMSA hydrogel and ES in promoting structural repair after TBI. Specifically, the TBI + hydrogel + ES group exhibited a 78.24% reduction in tissue loss compared to the untreated TBI group (Fig. 7J). To further investigate the regeneration of neural fibers and synapses, we performed Bielschowsky's silver staining (fig. S48). At 28 dpi, the untreated TBI group exhibited minimal evidence of regenerating neural fibers or synaptic structures, indicating limited spontaneous recovery of the neural network. In comparison, the TBI + hydrogel + ES group exhibited a notably higher density of regenerating neural fibers at 28 dpi, with a more organized structure, implying effective neural regeneration and structural remodeling. As summarized in Fig. 7k, fig. S49 and table S2 show that the combined treatment of hydrogel and ES demonstrates a notable synergistic effect, surpassing the outcomes of individual therapies. This strategy achieves in situ recruitment of endogenous NSCs and promotes their directional differentiation by modulating pathological features (such as neuroinflammation, glial scar formation, and vascular regeneration). Consequently, it accelerates axonal regeneration, myelination, and synaptic remodeling, ultimately facilitating the reconstruction of neural circuits and functional recovery after TBI.

Electrical signal recording after TBI treatment with LMSA hydrogel + ES

TBI causes direct neuronal damage and disrupts electrophysiological signaling. Subsequent ischemia and hypoxia further exacerbate this impairment, leading to abnormal brain electrical activity and altered oscillatory rhythms (*52*). These pathophysiological changes make neural activity monitoring particularly valuable for assessing early injuries. ECoG electrode, which records electrical signals directly from the cortical surface, offers superior spatial resolution and signal fidelity compared to scalp EEG, providing unique insights into the neural dynamics associated with TBI. In severe cases, ECoG captures characteristic electrophysiological disturbances, such as epileptiform discharges (EDs) and spreading depolarizations (SDs), both of which are closely linked to the extent of neural injury and clinical outcomes (*53*). EDs, a hallmark ECoG feature in TBI, are manifest heterogeneously as ictal rhythms, periodic spike-wave discharges, or rhythmic δ activity. Post-TBI seizures exhibit a bimodal temporal pattern: Early-phase events correlate with acute structural damage, whereas late-phase episodes are often driven by secondary neuroinflammation and maladaptive neural remodeling (*54*). SDs represent another critical ECoG phenomenon in TBI, characterized by slowly propagating waves of sustained depolarization that induce widespread neuronal and glial dysfunction (*55*). In ECoG recordings, SDs manifest as high-amplitude negative DC shifts followed by prolonged suppression of cortical activity. These electrophysiological events are closely linked to critical secondary injury mechanisms, including metabolic failure, excitotoxic damage, and disruption of the blood-brain barrier. Clinical evidence indicates that SDs occur most frequently within the early phase of TBI (24 to 48 hours), coinciding with the critical window for secondary damage progression (*56*). This temporal association underscores the potential of early SD-targeted interventions to improve clinical outcomes. ES has emerged as a promising modality for mitigating secondary injury processes in TBI (*48*, *57*).

In our study, we applied ES during the early postinjury phase (days 2 to 6), delivering treatment consecutively over 5 days. By recording ECoG signals at multiple time points following TBI, we evaluated the effect of ES on functional recovery and injury progression. On the basis of analysis of ECoG signals and their time-frequency representations (Fig. 8, A and B), both the TBI + ES and TBI + hydrogel + ES groups exhibited alternating episodes of EDs and SDs on day 1, reflecting severe neural impairment at this acute phase. However, by days 7, 14, and 21, the TBI + hydrogel + ES group showed a marked reduction in SD frequency compared to the TBI + ES group. Concurrently, epileptiform activity in the combined treatment group was characterized by lower signal amplitude and longer interdischarge intervals. During various stages post-TBI, the TBI + hydrogel + ES group exhibits an elevated power spectral density in the high-frequency region (80 to 150 Hz), indicating a high signal quality for evaluating the functional recovery (fig. S50). These electrophysiological improvements suggest that the hydrogel combined with ES confers enhanced neuroprotection, attenuates secondary injury progression, and contributes to improved functional recovery. Furthermore, time-frequency analysis of ECoG signals offers a quantitative framework for assessing TBI severity and predicting recovery trajectories in rodent models (fig. S51) (*58*). TBI disrupts thalamocortical circuitry, leading to a characteristic electrophysiological shift: Enhanced low-frequency (δ/θ) oscillations coupled with suppressed high-frequency (α/β) activity (*58*, *59*). Spectral analysis further reveals that subjects with dominant α-β rhythms generally experience more favorable outcomes, whereas those exhibiting predominant slow-wave activity tend to have poorer recovery. These spectral changes can be quantified using the δ + θ/α + β ratio—defined as the total power in the δ and θ bands divided by the combined

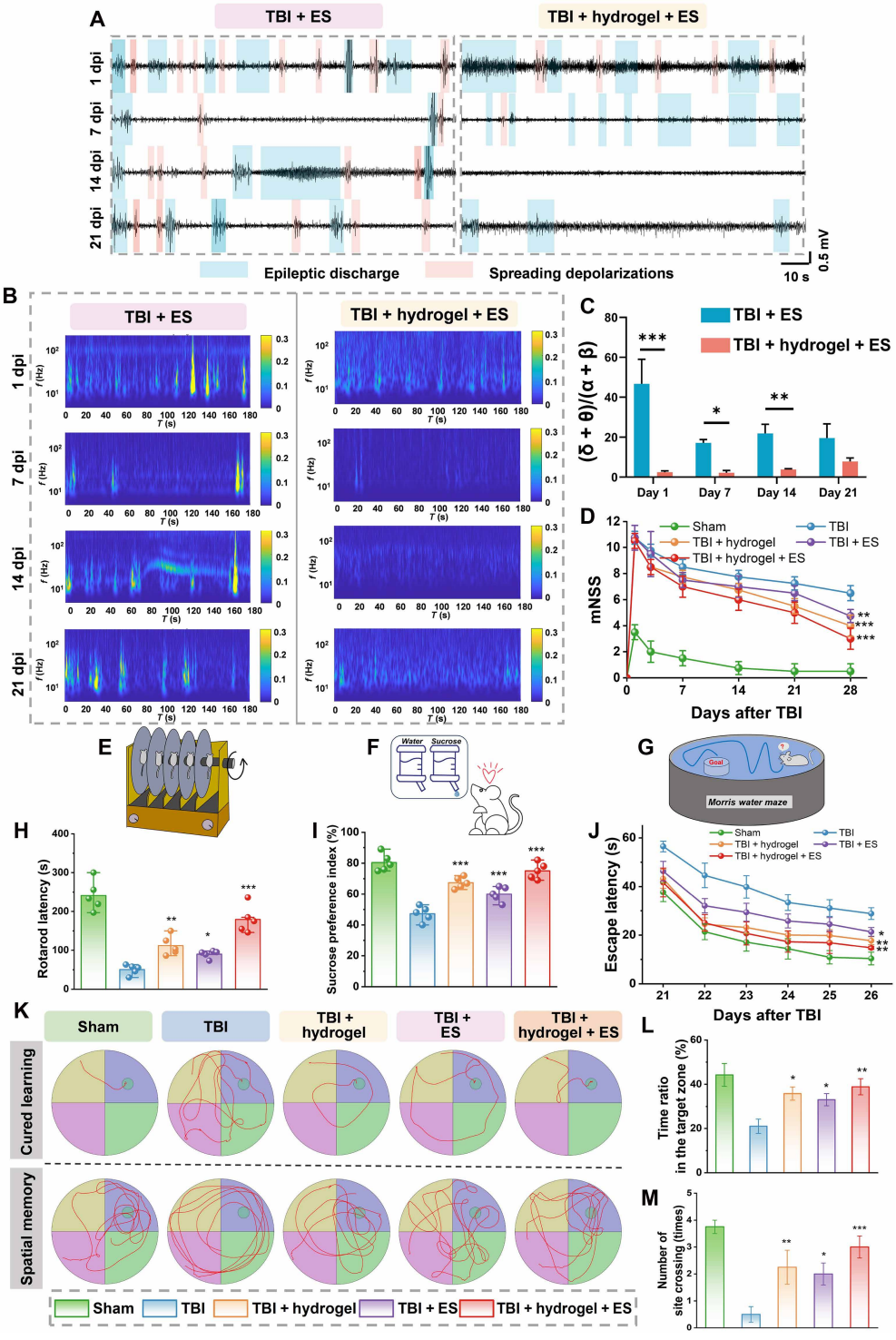

Fig. 8. ECoG analysis and neural functional recovery following TBI. (**A**) Representative 3-min ECoG traces at indicated time points post-TBI. EDs and SDs are highlighted in blue and red, respectively. (**B**) Time-frequency representations of ECoG signals derived through wavelet transform analysis. (**C**) Temporal evolution of the $\delta + \theta/\alpha + \beta$ power ratio ($n = 3$). (*$P < 0.05$, **$P < 0.01$, ***$P < 0.001$). (**D**) mNSS score to examine the neurological motor function recovery in rats ($n = 5$). (**E** and **H**) Rotarod test for evaluating motor coordination and balance in rats ($n = 5$). (**F** and **I**) Sucrose preference test for evaluating emotional behavior in rats ($n = 5$). (**G** and **J** to **M**) Representative swimming paths of rats during the learning and spatial memory phases (K), escape latency (J), time ratio in the target zone (I), and number of site crossings (M) measured by Morris water maze ($n = 5$). (*$P < 0.05$, **$P < 0.01$, and ***$P < 0.001$ compared to the TBI group).

power in the α and β bands. This ratio serves as a robust prognostic biomarker: Elevated values are associated with delayed consciousness recovery and a worse prognosis, while lower ratios correlate with accelerated neurological recovery and improved functional outcomes. The TBI + hydrogel + ES group exhibited a consistently lower δ + θ/α + β ratio than the TBI + ES group across all evaluated time points (days 1, 7, 14, and 21; Fig. 8C). The sustained reduction in this ratio suggests that the combined hydrogel and ES therapy effectively preserves thalamocortical function and mitigates the progression of secondary injury, thereby contributing to enhanced neurobehavioral recovery after TBI.

Neural function recovery ability and in vivo safety of the LMSA hydrogel + ES

Neurological recovery in TBI rats was systematically evaluated using the modified neurological severity score (mNSS), a comprehensive index of motor, sensory, reflex, and balance functions. As shown in Fig. 8D and fig. S52, compared to the TBI group and the single-treatment groups, the TBI + hydrogel + ES group exhibited a more pronounced reduction in mNSS scores at all time points, indicating superior recovery of motor function. The rotarod test further confirmed improvements in motor coordination and balance (Fig. 8, E and H, and fig. S53), with the TBI + hydrogel + ES group showing significantly prolonged latency to fall and a reduced number of falls. Regarding emotional behavior, the sucrose preference test revealed that the TBI group showed a low sucrose preference index, whereas all treatment groups showed improved sucrose preference (Fig. 8, F and I). Notably, the TBI + hydrogel + ES group demonstrated the most significant improvement, suggesting its advantage in alleviating depression-like behaviors. To assess cognitive function recovery, we conducted the Morris water maze test between 21 and 27 dpi (Fig. 8G). As shown in Fig. 8 (J and K) and fig. S54, during the 6-day training period, all treatment groups exhibited reduced escape latency compared to the TBI group, indicating a restored learning capacity. Among them, the TBI + hydrogel + ES group showed the shortest escape latency, indicating superior spatial learning ability. In the spatial probe test conducted at 27 dpi (Fig. 8, K, L, and M), the TBI + hydrogel + ES group spent the longest time in the target quadrant and crossed the former platform location most frequently, demonstrating significantly better spatial memory than other treatment groups. These results collectively suggest that the combination of hydrogel and ES effectively promotes cognitive recovery following TBI.

To evaluate the biosafety of the proposed treatment strategy, we performed H&E staining of major organs (heart, liver, spleen, lung, and kidney) and analyzed hematological parameters. As shown in fig. S55, at both 14 and 28 dpi, no notable pathological changes were observed in the major organs of any treatment group, with tissue architecture comparable to that of the normal group. Hematological parameters remained within normal ranges (fig. S56), indicating that the materials and ES methods used in this study exhibit good biocompatibility and in vivo safety.

DISCUSSION

In this work, we developed an injectable, conductive PolyLA-based adhesive hydrogel (LMSA) from clinically approved LA and Met, via a strategy of multi-hydrogen bond–driven supramolecular self-assembly precisely controlled by solution pH. Integrated with a flexible ECoG electrode, this system was applied for TBI treatment. The hydrogel exhibited brain tissue–matched mechanical strength and electrical conductivity. At the same time, its universal adhesion to wet tissues could facilitate seamless integration with brain surfaces and stable electrode coupling—effectively addressing the poor biocompatibility and low conduction efficiency of conventional electrodes. By integrating LA, Met, and ES within a unified system, the LMSA hydrogel achieved a paradigm shift from passive structural support to active adaptive neutral microenvironment reprogramming. Specifically, the sustained local release of LA and Met from LMSA hydrogel served distinct yet complementary roles: Met facilitated endogenous NSC recruitment, and LA remodeled the hostile niche to support neuronal differentiation. Ultimately, when combined with exogenous ES, this strategy notably enhanced neurogenesis and functional repair. The integrated platform also allowed for the transmission and recording of local electrophysiological signals, which facilitated real-time monitoring and accurate assessment of functional recovery during TBI repair. This hydrogel + ES combined strategy overcame key limitations of exogenous NSC transplantation, including difficult extraction, immune rejection, low survival rates, poor differentiation efficiency, and nondirectional differentiation property. Cellular and histological analyses provided compelling evidence that this synergistic strategy exerts a superior proneuronal differentiation effect, while behavioral assessments demonstrated marked improvements in motor function, emotional regulation, and cognitive performance in a rat model of TBI. In summary, this study proposes an integrated strategy that combines TBI repair with neural function assessment, providing a robust theoretical foundation and technical support for clinical interventions in TBI, while also establishing a critical prerequisite for the development of feedback-controlled neuromodulation systems. Future research will focus on establishing a correlation model between ECoG signal features and neural functional states, developing simplified feedback control algorithms, and enabling dynamic adjustment of ES parameters, thereby advancing the systematization and practical application of feedback-controlled neuromodulation protocols.

MATERIALS AND METHODS

Materials

LA (99%, Macklin, Shanghai, China) and Met (95%, Meryer, Shanghai, China) were used as received. All the other reagents are of analytical grade and used without further purification. The water used here was purified by a Utop ultrapure water machine with 100 W of power.

Preparation of LMSA hydrogels

LA and Met at different mass ratios were mixed first and then thoroughly dispersed in 1 ml of ultrapure water under vortexing. Then, the mixture was heated with a heating gun to form a transparent solution, followed by gelation at 37°C, resulting in bright-yellow LMSA hydrogels.

Characterization of LMSA hydrogels

FTIR spectrometry (PerkinElmer Spectrum 100, USA) was used to characterize the structure of LMSA hydrogels. The crystal structures of the LA powder, Met powder, and LMSA hydrogels were determined using XRD (D8 Advanced, Bruker, Germany). XRD data were obtained from 5° to 50° (2θ) using Cu Kα radiation with a scan

rate of 1° min^{-1}. Raman spectra were recorded on a DXR Microscope with 532-nm excitation. UV-Vis absorption spectra of the monomer release ratio, and DPPH and ABTS scavenging efficiency were recorded using a UV-Vis spectrometer (Genesys 180, Thermo Fisher Scientific). ITC experiments were performed using a TA Instruments NANO-ITC calorimeter at 298 K.

Rheology test

The rheological properties of LMSA hydrogels were measured using an Anton Paar MCR302 rheometer (Austria). Time-sweep tests were conducted at 37°C, with a strain of 0.1% and a frequency of 1 Hz. The angular frequency sweep test was conducted at 37°C with a strain of 1%, and the sample's storage modulus was recorded over the angular frequency range of 0.1 to 100 rad/s. The viscosity-shear rate curve was obtained at 37°C to illustrate the shear-thinning property of the hydrogel, and the viscosity was recorded for shear rates ranging from 0.01 to 10 s^{-1}.

Swelling test

To determine the swelling properties, the hydrogel samples were incubated at 37°C in ACSF. Before incubation, the initial volume (V_0) of the hydrogels was recorded. At each time point during incubation, the volume (V_n) was measured. The swelling ratio was then calculated using the following formula

$$\text{Swelling ratio}\ (\%) = \frac{V_n}{V_0} \times 100\,\%$$

In vitro degradation test

The degradation of LMSA hydrogels was evaluated by measuring their residual weight. Record the initial mass of LMSA hydrogels as W_0 (grams), and each LMSA hydrogel was separately immersed in PBS containing 10 μM of GSH and ACSF. In addition, the medium was replaced every 12 hours. At a predetermined time, the samples were collected, the surface culture medium was wiped dry with filter paper, and then reweigh as W_t (grams). The mass remaining (%) was calculated as follows

$$\text{Mass remaining}\ (\%) = \frac{W_0}{W_t} \times 100\,\%$$

Isolation and culture of NSCs

The cerebral cortex was isolated from neonatal mice on postnatal day 1. The isolated tissue is then mechanically dissociated and enzymatically digested with StemPro Accutase (Thermo Fisher Scientific) to create a single-cell suspension. After centrifugation, the pellet was collected and resuspended in culture medium. The cells were then cultured in suspension. Upon the formation of neurospheres approximately 1 μm in diameter, the spheres were dissociated into single NSCs using Accutase for subsequent experiments. This neurobasal medium (Thermo Fisher Scientific) is supplemented with penicillin-streptomycin solution and specific mitogenic growth factors, including N-2 supplement (Thermo Fisher Scientific), B-27 supplement (Thermo Fisher Scientific), GlutaMAX supplement (Thermo Fisher Scientific), epidermal growth factor (Thermo Fisher Scientific), and basic fibroblast growth factor (Novoprotein), to promote the proliferation and self-renewal of NSCs.

Cell cytotoxicity and live/dead cell staining

PC12 cells (*Rattus norvegicus*) were used to evaluate the cytocompatibility of the hydrogel. The hydrogel was immersed in PC12 cell culture medium for 24 hours to prepare the extract. This extract was then diluted into a series of concentrations. PC12 cells were seeded in a 96-well plate and treated with the graded concentrations of the extract. After 24 hours of incubation, cell viability was assessed using the CCK-8 assay. To investigate the effects of electrical parameters on cell viability, NSCs were used as the experimental subjects and exposed to varying ES conditions. Cell viability was assessed 24 hours poststimulation using the CCK-8 assay.

To investigate the effects of electrical parameters on cell viability, PC12 cells were used as a neuronal model to investigate the effect of electric current on cell activity. The cells were seeded in 24-well plates at a density of 1×10^5 cells per well. After overnight incubation, the cells were subjected to ES for 1 hour with current amplitudes of 0, 20, 50, and 100 (other parameters remained unchanged). Then, the cell viability was measured using the CCK-8 assay 24 hours after stimulation.

For fluorescence staining, the cell treatment was the same as described in the CCK-8 assay. After incubation, the cells were detached with trypsin, centrifuged, resuspended, and incubated in Calcein-AM staining solution and propidium iodide staining solution. The cells were then centrifuged, washed with 1× PBS, resuspended, and immediately observed under a confocal laser-scanning microscope. Live cells exhibited green fluorescence, whereas dead cells showed red fluorescence.

Cell scratch assay

NSCs were seeded at a density of 5×10^5 cells ml^{-1} into scratch assay plugins in a 24-well plate. After 24 hours of culture, when the cells reached 100% confluence, the plugins were gently removed, and the medium was replaced with fresh medium either with or without LMSA gel extract. ES was then applied to the designated groups (ES and hydrogel + ES) for 1 hours using a signal generator. After 8 hours of incubation, cell migration was observed under a microscope, and the scratch area was quantified to evaluate the cell migration ability.

Transwell experiment

The transwell inserts were precoated with poly-L-lysine and fibronectin. Subsequently, NSCs at a density of 4×10^4 were seeded into each insert. After the cells attached, the culture medium in the lower chamber was replaced with the LMSA gel extract. Three days later, the cells were fixed with 4% paraformaldehyde (PFA) for 15 min at room temperature. Then, the cells on the upper surface of the membrane were gently removed with a cotton swab, and the cells that had migrated were observed after crystal violet staining.

Differentiation of NSCs

The NSCs were seeded on culture plates coated with poly-L-lysine and laminin in a 24-well plate. After the cells adhered to the wall, the culture medium was replaced with the appropriate differentiation medium, and the cells were subjected to ES. The ES parameters were set as follows: current, 50 μA; frequency, 130 Hz; and duty cycle, 35%. After 7 days of differentiation, the cells were dehydrated and fixed with 4% PFA containing 20% sucrose (Solarbio) and stained with βIII-tubulin and Nestin (Abcam). The constitutional immunofluorescence images were captured using a laser-scanning confocal microscope (SP8, Leica, Germany).

Establishment and treatment of the TBI model in rats

All the animal experiments complied with the guidelines of the Tianjin Medical Experimental Animal Care, and animal protocols

were approved by the Institutional Animal Care and Use Committee of Yi Shengyuan Gene Technology (Tianjin) Co. Ltd. (protocol number YSY-DWLL-2024810). Seventy-five adult male SD rats (200 to 220 g, Beijing Vital River Laboratory Animal Technology Co. Ltd) were randomly assigned to the following five groups: Sham, TBI, TBI + hydrogel, TBI + ES, and TBI + hydrogel + ES groups. TBI models were generated using a CCI device (68099 II Pricise Impactor-Brain, RWD Life Science Co. LTD). Rats were anesthetized with isoflurane and then fixed on a standard brain stereotactic instrument. The right parietal regions (4 mm lateral to the sagittal suture, 2 mm posterior to the coronal suture) of the rats' skulls were drilled through a miniature hand-held skull drill (RWD Life Science Company, China) to create a 5-mm diameter bone window. The impact parameters applied were as follows: the impactor tip diameter of 3 mm, a depth of 2.5 mm, a velocity of 4.5 m/s, and a dwell time of 120 ms. In the Sham group, rats were subjected to cranial window opening without any impact. In the TBI, TBI + hydrogel, TBI + ES, and TBI + hydrogel + ES groups, the cranial window was opened, and the impact was administered simultaneously. After the impact, 20 μl of physiological saline was then injected into the lesion site in the TBI group. In the TBI + hydrogel group, 20 μl of LMSA-0.25 hydrogel was then injected into the lesion site. In the TBI + ES group, electrodes were implanted at the lesion site without hydrogel injection. In the TBI + hydrogel + ES group, 20 μl of LMSA-0.25 hydrogel was injected into the lesion site, followed by the implantation of electrodes. Last, the wound was sutured and disinfected. All procedures were performed on a heated pad to maintain the rats' normal body temperature.

Neural signal recording

Neural activity was recorded weekly using a multichannel in vivo neural signal acquisition system (Cereplex Direct, Blackrock Microsystems) with a notch filter at 50 Hz. Electrophysiological signals were digitized at 30 kHz. LFP signals were obtained by downsampling the raw signals to 2000 Hz and applying low-pass filtering (0.1 to 200 Hz). The signals were further analyzed in MATLAB (The MathWorks Inc.) Butterworth band-pass filters, and the "filtfilt" function were used to filter the signals into five frequency bands: δ (1 to 4 Hz), θ (4 to 8 Hz), α (8 to 13 Hz), β (13 to 30 Hz), and γ (30 to 150 Hz). Band power in each frequency band was calculated using the bandpower function, and the power spectrum density was computed using the "pwelch" function.

In vivo ES

Biphasic, cathodal-first, charge-balanced constant-current pulses were delivered to the right sensorimotor cortex through the flexible ECoG electrode using a multichannel stimulus generator (STG 4004, Multi Channel Systems MCS GmbH). Unless otherwise specified, stimulation parameters were as follows: 50 μA, 130 Hz, duty cycle 0.35, 1 ms pulse width per phase. Each daily session consisted of five stimulation trains of 1-min ON separated by 3-min OFF intervals (total session duration: 20 min). ES started 2 days after model induction and was applied once daily for five consecutive days (days 2 to 6).

Histological and immunofluorescent staining

At 7, 14, and 28 dpi, rats were perfused with fixative after deep anesthesia for subsequent histological analysis. After 3 days of fixation with 4% PFA, brain tissue was paraffin-embedded and cut to obtain 5-μm-thick sections. H&E staining (Solarbio, China), Bielschowsky's silver staining (Solarbio, China), LFB staining (Solarbio, China), Nissl staining (Solarbio, China), and Masson staining (Solarbio, China) were performed to visualize cell infiltration, nerve fibers, myelin sheaths, neurons, and glial scars at the lesion site of TBI, respectively. For immunofluorescence staining, brain tissue sections were incubated with the following primary antibodies: Nestin (Solarbio, China, K009698P), Tuj-1 (Solarbio, China, K011585M), MBP (Solarbio, China, K009767M), GFAP (Solarbio, China, K106966P), NeuN (Solarbio, China, K009907M), Iba-1 (Solarbio, China, K011584M), GAP43 (Solarbio, China, K101307P), CD31 (Solarbio, China, K011574M), α-SMA (Solarbio, China, K109667P), NF (Solarbio, China, K009466P), CD86 (Solarbio, China, K010082P), and CD206 (Solarbio, China, K006619P). All antibodies were purchased from Beijing Solarbio Science & Technology Co. Ltd. Histological and immunofluorescence staining in this study were quantified using ImageJ (National Institutes of Health) software. Histological assessment was performed by a blinded pathologist, and representative images of each group were shown in the corresponding figures.

Statistical analysis

All experimental procedures included a minimum of three independent replicate samples for each group, with quantitative results expressed as means ± standard deviation throughout the study. The sample size (n) for each experimental group is specified in the respective figure legends. Data from experiments were analyzed using GraphPad Prism 8.0 software. One-way analysis of variance (ANOVA) followed by Tukey's post hoc test was used to compare multiple groups.

Supplementary Materials

This PDF file includes:

Supplementary Materials and Methods
Figs. S1 to S56
Tables S1 and S2
References

REFERENCES

1. T. L. Roth, D. Nayak, T. Atanasijevic, A. P. Koretsky, L. L. Latour, D. B. McGavern, Transcranial amelioration of inflammation and cell death after brain injury. *Nature* **505**, 223–228 (2014).
2. A. A. B. Jamjoom, J. Rhodes, P. J. D. Andrews, S. G. N. Grant, The synapse in traumatic brain injury. *Brain* **144**, 18–31 (2021).
3. V. B. Risbrough, M. N. Vaughn, S. F. Friend, Role of inflammation in traumatic brain injury–associated risk for neuropsychiatric disorders: State of the evidence and where do we go from here. *Biol. Psychiatry* **91**, 438–448 (2022).
4. H. Xia, W. Zhou, D. Li, F. Peng, C. Wang, L. Yu, J. Du, Y. Zheng, Y. Sang, Y. Zhang, L. Han, H. Liu, A. Hao, J. Qiu, Engineering neural stem cells with micropatches for improved therapy of traumatic brain injury. *Angew. Chem. Int. Ed. Engl.* **64**, e202512804 (2025).
5. L. Liang, X. Li, K. Hu, P. Cai, J. Wang, J. Yu, S. Wang, Y. Zhao, C. Xu, S. Li, H. Liu, C. Wang, J. Zhou, Neuroimmune microenvironment reprogramming via immuno-piezoelectric transducers for synergistic stem cell therapy in traumatic brain injury. *Adv. Mater.* **38**, e12810 (2026).
6. H. Yang, H. Liu, C. Lou, M. Han, Z. Sun, Y. Su, K. Bian, D. Zhao, Y. Li, Y. Sang, C. Liu, Z. Geng, H. Liu, J. Qiu, Flexible living artificial dura mater for efficient therapy of central nervous system injury based on neuronal differentiation and neuroprotective A2 astrocyte activation. *Adv. Mater.* **37**, e11878 (2025).
7. W. Wang, K. Li, W. Ma, Y. Li, F. Liu, Y. Kong, L. Wang, F. Yi, Y. Sang, G. Li, H. Liu, J. Qiu, Ultrasound-activated piezoelectric nanostickers for neural stem cell therapy of traumatic brain injury. *Nat. Mater.* **24**, 1137–1150 (2025).
8. M. Ronaghi, S. Erceg, V. Moreno-Manzano, M. Stojkovic, Challenges of stem cell therapy for spinal cord injury: Human embryonic stem cells, endogenous neural stem cells, or induced pluripotent stem cells? *Stem Cells* **28**, 93–99 (2010).
9. C.-C. Ke, R.-S. Liu, A. Suetsugu, H. Kimura, J. H. Ho, O. K. Lee, R. M. Hoffman, In vivo fluorescence imaging reveals the promotion of mammary tumorigenesis by mesenchymal stromal cells. *PLOS ONE* **8**, e69658 (2013).

10. W. Chi, Y. He, S. Chen, L. Guo, Y. Yuan, R. Li, R. Liu, D. Zhou, J. Du, T. Xu, Y. Yu, Advances in research on biomaterials and stem cell/exosome-based strategies in the treatment of traumatic brain injury. *Acta Pharm. Sin. B* **15**, 3511–3544 (2025).
11. D. Xiao, Y. Sun, G. Yang, W. Yan, M. Jiang, Z. Qin, Z. Wang, Y. Gu, J. Zhou, J. Tan, G. Li, Y. Li, C. Zhu, Nonexpansive biodegradable matrix promotes blood vessel organoid development for neurovascular repair and functional recovery in ischaemic stroke. *Nat. Biomed. Eng.*, 10.1038/s41551-025-01550-1 (2025).
12. N. V. Phan, E. M. Rathbun, Y. Ouyang, S. T. Carmichael, T. Segura, Biology-driven material design for ischaemic stroke repair. *Nat. Rev. Bioeng.* **2**, 44–63 (2024).
13. J. Marschallinger, T. Iram, M. Zardeneta, S. E. Lee, B. Lehallier, M. S. Haney, J. V. Pluvinage, V. Mathur, O. Hahn, D. W. Morgens, J. Kim, J. Tevini, T. K. Felder, H. Wolinski, C. R. Bertozzi, M. C. Bassik, L. Aigner, T. Wyss-Coray, Lipid-droplet-accumulating microglia represent a dysfunctional and proinflammatory state in the aging brain. *Nat. Neurosci.* **23**, 194–208 (2020).
14. Y. Luo, P. Jiang, D. Huang, H. Li, J. He, R. Shen, Y. Jiang, L. Rong, B. Liu, Synergistic mitochondrial homeostasis regulation and cholinergic circuits reconstruction via a one-step synthesized multifunctional hydrogel facilitates spinal cord injury repair. *Bioact. Mater.* **59**, 370–395 (2026).
15. N. Wu, S. Wan, S. Su, H. Huang, G. Dou, L. Sun, Electrode materials for brain–machine interface: A review. *InfoMat* **3**, 1174–1194 (2021).
16. X. Wang, X. Sun, D. Gan, M. Soubrier, H.-Y. Chiang, L. Yan, Y. Li, J. Li, S. Yu, Y. Xia, K. Wang, Q. Qin, X. Jiang, L. Han, T. Pan, C. Xie, X. Lu, Bioadhesive and conductive hydrogel-integrated brain-machine interfaces for conformal and immune-evasive contact with brain tissue. *Matter* **5**, 1204–1223 (2022).
17. Q. Wang, H. Wang, Y. Ma, X. Cao, H. Gao, Effects of electroactive materials on nerve cell behaviors and applications in peripheral nerve repair. *Biomater. Sci.* **10**, 6061–6076 (2022).
18. C. M. Tran, Z. Yue, C. Qin, K. B. C. Imani, M. Dottori, R. J. Forster, G. G. Wallace, 3D printing of conducting polymer hydrogels for electrostimulation-assisted tissue engineering. *Adv. Mater.* **37**, e2507779 (2025).
19. Y. Bai, H. Meng, Z. Li, Z. L. Wang, Degradable piezoelectric biomaterials for medical applications. *MedMat* **1**, 40–49 (2024).
20. L. Wang, J. Du, Q. Liu, D. Wang, W. Wang, M. Lei, K. Li, Y. Li, A. Hao, Y. Sang, F. Yi, W. Zhou, H. Liu, C. Mao, J. Qiu, Wrapping stem cells with wireless electrical nanopatches for traumatic brain injury therapy. *Nat. Commun.* **15**, 7223 (2024).
21. Z. Yang, Y. You, X. Liu, Q. Wan, Z. Xu, Y. Shuai, J. Wang, T. Guo, J. Hu, J. Lv, M. Zhang, M. Yang, C. Mao, S. Yang, Injectable Bombyx mori (B. mori) silk fibroin/MXene conductive hydrogel for electrically stimulating neural stem cells into neurons for treating brain damage. *J. Nanobiotechnology* **22**, 111 (2024).
22. O. Ameen, R. M. Samaka, R. A. A. Abo-Elsoud, Metformin alleviates neurocognitive impairment in aging via activation of AMPK/BDNF/PI3K pathway. *Sci. Rep.* **12**, 17084 (2022).
23. K. Liu, L. Li, Z. Liu, G. Li, Y. Wu, X. Jiang, M. Wang, Y. Chang, T. Jiang, J. Luo, J. Zhu, H. Li, Y. Wang, Acute administration of metformin protects against neuronal apoptosis induced by cerebral ischemia-reperfusion injury via regulation of the AMPK/CREB/BDNF pathway. *Front. Pharmacol.* **13**, 832611 (2022).
24. T. Yuan, T. Wang, J. Zhang, P. Liu, J. Xu, Z. Gu, J. Xu, Y. Li, Robust and multifunctional nanoparticles assembled from natural polyphenols and metformin for efficient spinal cord regeneration. *ACS Nano* **17**, 18562–18575 (2023).
25. Y. Yang, W. Zhang, S. Pei, J. Shao, W. Huang, X. Gao, Theoretical study of the N-H···O red-shifted and blue-shifted hydrogen bonds. *Sci. China Ser. B Chem.* **50**, 32–40 (2007).
26. H. Song, F. Fu, Y. Chen, R. Yang, Z. Luo, J. Shao, Y. Qi, Q. Zhang, J. Wang, H. Sun, C. Cui, W. Liu, A poly(lipoic acid)-based elastomer adhesive with synergistic activity of microenvironment regulation and peripheral neuropathy repair facilitates infectious diabetic wound healing. *Biomaterials* **324**, 123489 (2026).
27. Z. Zhang, Y. Xia, X. Li, Q. Zhang, Y. Wu, C. Cui, J. Liu, W. Liu, Arginine-solubilized lipoic acid-induced β-sheets of silk fibroin-strengthened hydrogel for postoperative rehabilitation of breast cancer. *Bioact. Mater.* **40**, 667–682 (2024).
28. W. Pi, L. Wu, J. Lu, X. Lin, X. Huang, Z. Wang, Z. Yuan, H. Qiu, J. Zhang, H. Lei, P. Wang, A metal ions-mediated natural small molecules carrier-free injectable hydrogel achieving laser-mediated photo-Fenton-like anticancer therapy by synergy apoptosis/cuproptosis/anti-inflammation. *Bioact. Mater.* **29**, 98–115 (2023).
29. G. Yang, Y. Liu, S. R. Devkota, Y. Hui, R. Zhao, Y. Li, D. A. Weitz, C. Zhao, A sustainable biotechnology approach for mineral separation. *Adv. Funct. Mater.* **35**, e04992 (2025).
30. W. Fu, M. Guo, X. Zhou, Z. Wang, J. Sun, Y. An, T. Guan, M. Hu, J. Li, Z. Chen, J. Ye, X. Gao, G. F. Gao, L. Dai, Y. Wang, C. Chen, Injectable hydrogel mucosal vaccine elicits protective immunity against respiratory viruses. *ACS Nano* **18**, 11200–11216 (2024).
31. X. Tian, P. Wang, T. Li, X. Huang, W. Guo, Y. Yang, M. Yan, H. Zhang, D. Cai, X. Jia, F. Li, B. Xu, T. Ma, C. Yan, H. Lei, Self-assembled natural phytochemicals for synergistically antibacterial application from the enlightenment of traditional Chinese medicine combination. *Acta Pharm. Sin. B* **10**, 1784–1795 (2020).
32. Y. Qi, C. Xu, Z. Zhang, Q. Zhang, Z. Xu, X. Zhao, Y. Zhao, C. Cui, W. Liu, Wet environment-induced adhesion and softening of coenzyme-based polymer elastic patch for treating periodontitis. *Bioact. Mater.* **35**, 259–273 (2024).
33. Z. Luo, Q. Zhao, Y. Zhang, J. Shao, Y. Zhao, M. Li, Y. Dou, C. Cui, Q. Yang, W. Liu, Coral-inspired bioactive porous adhesive for fractured bone repair. *Adv. Funct. Mater.* **35**, 2507592 (2025).
34. E. Moeendarbary, I. P. Weber, G. K. Sheridan, D. E. Koser, S. Soleman, B. Haenzi, E. J. Bradbury, J. Fawcett, K. Franze, The soft mechanical signature of glial scars in the central nervous system. *Nat. Commun.* **8**, 14787 (2017).
35. B. Shen, J. Wang, T. He, S. Chen, X. Wang, J. Chen, R. Shi, J. Wang, H. Wang, W. Huang, C. Cao, X. Tan, J. Nam, L. Lin, Ultrasoft bioadhesive hydrogel as a versatile platform for the delivery of basic fibroblast growth factor to repair traumatic brain injury. *Chem. Eng. J.* **483**, 149017 (2024).
36. J. Teichert, R. Hermann, P. Ruus, R. Preiss, Plasma kinetics, metabolism, and urinary excretion of alpha-lipoic acid following oral administration in healthy volunteers. *J. Clin. Pharmacol.* **43**, 1257–1267 (2003).
37. P. Theodosis-Nobelos, G. Papagiouvannis, P. Tziona, E. A. Rekka, Lipoic acid. Kinetics and pluripotent biological properties and derivatives. *Mol. Biol. Rep.* **48**, 6539–6550 (2021).
38. Y. Chen, M. Yu, M. Liu, Y. Sun, C. Ling, M. Yu, W. Zhang, W. Zhang, X. Peng, A solvent exchange induced robust wet adhesive hydrogels to treat solid tumor through synchronous ethanol ablation and chemotherapy. *Adv. Sci.* **11**, e2309760 (2024).
39. H. Song, Y. Qi, Z. Luo, J. Shao, C. Cui, W. Liu, A salt-bridge hydrogen bond stabilized poly(lipoic acid)-based bioactive adhesive. *Sci. China Technol. Sci.* **68**, 1720201 (2025).
40. C. Cui, L. Mei, D. Wang, P. Jia, Q. Zhou, W. Liu, A self-stabilized and water-responsive deliverable coenzyme-based polymer binary elastomer adhesive patch for treating oral ulcer. *Nat. Commun.* **14**, 7707 (2023).
41. C. Cui, Y. Sun, X. Nie, X. Yang, F. Wang, W. Liu, A coenzyme-based deep eutectic supramolecular polymer bioadhesive. *Adv. Funct. Mater.* **33**, 2307543 (2023).
42. X. Zhao, F. Wang, Y. Sun, R. Yang, Z. Luo, W. Liu, C. Cui, An in situ self-solidifying poly(lipoic-acid) liquid adhesive forms pathogen-resistant barrier for ulcerative colitis therapy. *ACS Nano* **19**, 40222–40244 (2025).
43. Y. Qi, J. Shao, Z. Luo, Q. Zhang, X. Tian, R. Yang, Y. Sun, D. Chen, C. Cui, W. Liu, In vivo adhesion fault-tolerant coenzyme/queen bee acid nanomicelles self-crosslinked thermoresponsive adhesive hydrogel for efficient oral ulcer treatment. *Bioact. Mater.* **52**, 460–473 (2025).
44. L. Yan, S. Liu, J. Wang, X. Ding, Y. Zhao, N. Gao, Z. Xia, M. Li, Q. Wei, O. V. Okoro, Y. Sun, L. Nie, A. Shavandi, G. Jiang, J. Chen, L. Fan, Y. Weng, Constructing nerve guidance conduit using dECM-doped conductive hydrogel to promote peripheral nerve regeneration. *Adv. Funct. Mater.* **34**, 2402698 (2024).
45. M. Yang, L. Wang, W. Liu, W. Li, Y. Huang, Q. Jin, L. Zhang, Y. Jiang, Z. Luo, Highly-stable, injectable, conductive hydrogel for chronic neuromodulation. *Nat. Commun.* **15**, 7993 (2024).
46. S. Jin, H. Choi, D. Seong, C.-L. You, J.-S. Kang, S. Rho, W. B. Lee, D. Son, M. Shin, Injectable tissue prosthesis for instantaneous closed-loop rehabilitation. *Nature* **623**, 58–65 (2023).
47. D. J. Guggenmos, M. Azin, S. Barbay, J. D. Mahnken, C. Dunham, P. Mohseni, R. J. Nudo, Restoration of function after brain damage using a neural prosthesis. *Proc. Natl. Acad. Sci. U.S.A.* **110**, 21177–21182 (2013).
48. N. D. Schiff, J. T. Giacino, C. R. Butson, E. Y. Choi, J. L. Baker, K. P. O'Sullivan, A. P. Janson, M. Bergin, H. M. Bronte-Stewart, J. Chua, L. DeGeorge, S. Dikmen, A. Fogarty, L. M. Gerber, M. Krel, J. Maldonado, M. Radovan, S. A. Shah, J. Su, N. Temkin, T. Tourdias, J. D. Victor, A. Waters, S. A. Kolakowsky-Hayner, J. J. Fins, A. G. Machado, B. K. Rutt, J. M. Henderson, Thalamic deep brain stimulation in traumatic brain injury: A phase 1, randomized feasibility study. *Nat. Med.* **29**, 3162–3174 (2023).
49. S. F. Cogan, Neural stimulation and recording electrodes. *Annu. Rev. Biomed. Eng.* **10**, 275–309 (2008).
50. F. Han, X. Ma, Y. Zhai, L. Cui, L. Yang, Z. Zhu, Y. Hao, G. Cheng, Strategy for designing a cell scaffold to enable wireless electrical stimulation for enhanced neuronal differentiation of stem cells. *Adv. Healthc. Mater.* **10**, e2100027 (2021).
51. Z. Liu, X. Wan, Z. L. Wang, L. Li, Electroactive biomaterials and systems for cell fate determination and tissue regeneration: Design and applications. *Adv. Mater.* **33**, e2007429 (2021).
52. C. Werner, K. Engelhard, Pathophysiology of traumatic brain injury. *Br. J. Anaesth.* **99**, 4–9 (2007).
53. R. Di Sapia, M. Rizzi, F. Moro, I. Lisi, A. Caccamo, T. Ravizza, A. Vezzani, E. R. Zanier, ECoG spiking activity and signal dimension are early predictive measures of epileptogenesis in a translational mouse model of traumatic brain injury. *Neurobiol. Dis.* **185**, 106251 (2023).
54. R. D'Ambrosio, Post-traumatic epilepsy following fluid percussion injury in the rat. *Brain* **127**, 304–314 (2004).
55. J. P. Dreier, The role of spreading depression, spreading depolarization and spreading ischemia in neurological disease. *Nat. Med.* **17**, 439–447 (2011).
56. M. A. MacLean, J. H. Muradov, R. Greene, G. Van Hameren, D. B. Clarke, J. P. Dreier, D. O. Okonkwo, A. Friedman, Memantine inhibits cortical spreading depolarization and improves neurovascular function following repetitive traumatic brain injury. *Sci. Adv.* **9**, eadj2417 (2023).
57. N. D. Schiff, J. T. Giacino, K. Kalmar, J. D. Victor, K. Baker, M. Gerber, B. Fritz, B. Eisenberg, J. O'Connor, E. J. Kobylarz, S. Farris, A. Machado, C. McCagg, F. Plum, J. J. Fins, A. R. Rezai,

Behavioural improvements with thalamic stimulation after severe traumatic brain injury. *Nature* **448**, 600–603 (2007).
58. P. E. Rapp, D. O. Keyser, A. Albano, R. Hernandez, D. B. Gibson, R. A. Zambon, W. D. Hairston, J. D. Hughes, A. Krystal, A. S. Nichols, Traumatic brain injury detection using electrophysiological methods. *Front. Hum. Neurosci.* **9**, 11 (2015).
59. R. J. Fenster, L. A. M. Lebois, K. J. Ressler, J. Suh, Brain circuit dysfunction in post-traumatic stress disorder: From mouse to man. *Nat. Rev. Neurosci.* **19**, 535–551 (2018).
60. J. Guo, S. Zhang, Y. Tao, B. Fan, W. Tang, Glutathione-triggered biodegradable poly(disulfide)s: Ring-opening copolymerization and potent antibacterial activity. *Polym. Chem.* **13**, 6637–6649 (2022).
61. X. Huang, Y. Ye, J. Zhang, X. Zhang, H. Ma, Y. Zhang, X. Fu, J. Tang, N. Jiang, Y. Han, H. Liu, H. Chen, Reactive oxygen species scavenging functional hydrogel delivers procyanidins for the treatment of traumatic brain injury in mice. *ACS Appl. Mater. Interfaces* **14**, 33756–33767 (2022).
62. Y. Zheng, G. Wu, L. Chen, Y. Zhang, Y. Luo, Y. Zheng, F. Hu, T. Forouzanfar, H. Lin, B. Liu, Neuro-regenerative imidazole-functionalized GelMA hydrogel loaded with hAMSC and SDF-1α promote stem cell differentiation and repair focal brain injury. *Bioact. Mater.* **6**, 627–637 (2021).
63. X. Liu, C. Wu, Y. Zhang, S. Chen, J. Ding, Z. Chen, K. Wu, X. Wu, T. Zhou, M. Zeng, D. Wei, J. Sun, H. Fan, L. Zhou, Hyaluronan-based hydrogel integrating exosomes for traumatic brain injury repair by promoting angiogenesis and neurogenesis. *Carbohydr. Polym.* **306**, 120578 (2023).
64. F. Qian, Y. Han, Z. Han, D. Zhang, L. Zhang, G. Zhao, S. Li, G. Jin, R. Yu, H. Liu, In situ implantable, post-trauma microenvironment-responsive, ROS depletion hydrogels for the treatment of traumatic brain injury. *Biomaterials* **270**, 120675 (2021).
65. Y. Chai, H. Zhao, S. Yang, X. Gao, Z. Cao, J. Lu, Q. Sun, W. Liu, Z. Zhang, J. Yang, X. Wang, T. Chen, X. Kong, A. G. Mikos, X. Zhang, Y. Zhang, X. Wang, Structural alignment guides oriented migration and differentiation of endogenous neural stem cells for neurogenesis in brain injury treatment. *Biomaterials* **280**, 121310 (2022).
66. Y. Hu, Y. Jia, S. Wang, Y. Ma, G. Huang, T. Ding, D. Feng, G. M. Genin, Z. Wei, F. Xu, An ECM-mimicking, injectable, viscoelastic hydrogel for treatment of brain lesions. *Adv. Healthc. Mater.* **12**, e2201594 (2023).
67. C. Li, M. Kuss, Y. Kong, F. Nie, X. Liu, B. Liu, A. Dunaevsky, P. Fayad, B. Duan, X. Li, 3D printed hydrogels with aligned microchannels to guide neural stem cell migration. *ACS Biomater Sci. Eng.* **7**, 690–700 (2021).
68. L. Wang, D. Zhang, Y. Ren, S. Guo, J. Li, S. Ma, M. Yao, F. Guan, Injectable hyaluronic acid hydrogel loaded with BMSC and NGF for traumatic brain injury treatment. *Mater. Today Bio* **13**, 100201 (2022).
69. Y. Li, M. Wang, M. Sun, X. Wang, D. Pei, B. Lei, A. Li, Engineering antioxidant poly (citrate-gallic acid)-exosome hybrid hydrogel with microglia immunoregulation for traumatic brain injury-post neuro-restoration. *Compos. Part B Eng.* **242**, 110034 (2022).
70. T. Chen, Y. Xia, L. Zhang, T. Xu, Y. Yi, J. Chen, Z. Liu, L. Yang, S. Chen, X. Zhou, X. Chen, H. Wu, J. Liu, Loading neural stem cells on hydrogel scaffold improves cell retention rate and promotes functional recovery in traumatic brain injury. *Mater. Today Bio* **19**, 100606 (2023).
71. S. Yang, W. Luo, X. Song, Q. Chen, J. Liu, P. Gan, C. Liu, T. Li, G. Xu, Y. Zhang, J. Zheng, Y. Wang, A self-gelling powder directly co-assembled by natural small molecules for traumatic brain injury. *Adv. Funct. Mater.* **34**, 2401485 (2024).
72. W. Luo, X. Guo, X. Song, Q. Chen, J. Liu, C. Chen, X. Guo, X. Fan, J. Zheng, Z. Yuan, M. Cheng, H. Li, T. Tang, Y. Wang, Surgical-adjuvant hydrogel of full-natural bioactive compounds from Chinese medicine for enhanced traumatic brain injury therapy by inhibiting complement activation. *Adv. Funct. Mater.* **36**, e08893 (2026).
73. W. Luo, Z. Yang, J. Zheng, Z. Cai, X. Li, J. Liu, X. Guo, M. Luo, X. Fan, M. Cheng, T. Tang, J. Liu, Y. Wang, Small molecule hydrogels loading small molecule drugs from Chinese medicine for the enhanced treatment of traumatic brain injury. *ACS Nano* **18**, 28894–28909 (2024).
74. N. Hu, J.-X. Shi, C. Chen, H.-H. Xu, Z.-H. Chang, P.-F. Hu, D. Guo, X.-W. Zhang, W.-W. Shao, X. Fan, J.-C. Zuo, D. Ming, X.-H. Li, Constructing organoid-brain-computer interfaces for neurofunctional repair after brain injury. *Nat. Commun.* **15**, 9580 (2024).
75. R.-S. Hsu, S.-J. Li, J.-H. Fang, I.-C. Lee, L.-A. Chu, Y.-C. Lo, Y.-J. Lu, Y.-Y. Chen, S.-H. Hu, Wireless charging-mediated angiogenesis and nerve repair by adaptable microporous hydrogels from conductive building blocks. *Nat. Commun.* **13**, 5172 (2022).
76. J. Zhou, Y. Ran, C. Qiao, J. Liang, Y. Wang, W. Su, Y. Xiao, L. Ye, J. Xi, Z. Liu, In situ implantable and reactive oxygen species responsive hydrogel loaded with minocycline for functional rehabilitation of traumatic brain injury. *Chem. Eng. J.* **517**, 164322 (2025).
77. X. Liu, C. Wu, Y. Zhang, G. Li, S. Chen, Z. Chen, P. Liu, K. Wu, X. Wu, T. Zhou, M. Zeng, Z. Qiao, J. Xiao, J. Ding, D. Wei, J. Sun, J. Xu, L. Zhou, H. Fan, Viscoelastic cues to induce stem cell migration and neuronal differentiation in cell-free hydrogel-assisted TBI recovery. *Chem. Eng. J.* **492**, 152401 (2024).

Acknowledgments
Funding: We gratefully acknowledge the support for this work from the Brain Science and Brain-like Intelligence Technology-National Science and Technology Major Project (2021ZD0201602 to W.L.), the National Natural Science Foundation of China (52233008 to W.L., 52303201 and 52473143 to C.C., T2125003 and U25A20417 to Z. Li, and 52403212 to M.X.), and Beijing Natural Science Foundation (Z240022 and L245015 to Z. Li). The 10th CAST Young Talent Support Project (2025E8-0025 to C.C.). **Author contributions:** Conceptualization: Z. Luo, M.X., J.H., C.C., Z. Li, and W.L. Methodology: Z. Luo, M.X., and J.H. Investigation: Z. Luo, M.X., J.H., R.Y., X.Z., J.S., and J.C. Visualization: Z. Luo, M.X., and W.L. Resources: Z. Luo, J.C., and W.L. Data curation: Z. Luo. Validation: Z. Luo. Formal analysis: Z. Luo. Software: Z. Luo. Funding acquisition: W.L. Project administration: W.L. Supervision: C.C., Z. Li, and W.L. Writing—original draft: Z. Luo, M.X., and W.L. Writing—review and editing: Z. Luo, C.C., Z. Li, and W.L. **Competing interests:** The authors declare that they have no competing interests. **Data, code, and materials availability:** All data and code needed to evaluate and reproduce the results in the paper are present in the paper and/or the Supplementary Materials. The new material LMSA hydrogel produced in this paper is described in detail in the "Preparation of LMSA hydrogels" section of the Materials and Methods. Alternatively, requests for materials should be directed to the corresponding author, W.L. (wgliu@tju.edu.cn).

Submitted 9 January 2026
Accepted 17 April 2026
Published 29 May 2026
10.1126/sciadv.aef3388

ScienceAdvances

An antiswelling biodegradable hydrogel reshapes electro-microenvironment to drive endogenous neuroregeneration after brain defect

Zhen Luo, Meng Xiao, Jing Huang, Rong Yang, Xinrui Zhao, Jiaxing Shao, Jian Cheng, Chunyan Cui, Zhou Li, and Wenguang Liu

Sci. Adv. **12** (22), eaef3388. DOI: 10.1126/sciadv.aef3388